Chemical Science

Accepted Manuscript

This article can be cited before page numbers have been issued, to do this please use: J. Feng, S. Chen, Y. Wu, X. Huang and C. Yu, *Chem. Sci.*, 2026, DOI: 10.1039/D5SC09176D.

ROYAL SOCIETY OF CHEMISTRY

rsc.li/chemical-science

View Article Online
DOI: 10.1039/D5SC09176D

Recent Advances and Design Strategies of Cathode Materials for Aqueous Aluminum-Ion Batteries

Jiayou Feng, Shuimei Chen, Yuzheng Wu, Xiaodan Huang*, Chengzhong Yu*

Australian Institute for Bioengineering and Nanotechnology, The University of Queensland, Brisbane, QLD 4072, Australia

*Corresponding author, E-mail: x.huang@uq.edu.au; c.yu@uq.edu.au

Abstract

The growing global energy demand stimulates the urgent need for safe, sustainable, and cost-effective energy storage technologies. Aqueous aluminum-ion batteries (AAIBs) have emerged as promising candidates owing to their abundant resources, intrinsic safety, environmental compatibility, and high capacity. AAIBs research has seen rapid development, focusing on high-capacity cathodes compatible with Al anodes. The high charge density of trivalent Al^{3+} induces strong electrostatic interactions with the cathode, impeding ion transport, causing structural distortion, and accelerating capacity decay, while side reactions in aqueous electrolytes further limit reversibility and stability. Addressing these challenges requires a mechanistic understanding of how cathode composition and structure regulate Al^{3+}-cathode interactions and redox behavior. This review analyzes the fundamental Al^{3+} storage mechanisms in AAIBs, emphasizing the influence of cathode chemistry, structural characteristics, and electrolyte environment on ion transport, Al^{3+}-cathode interactions and electrochemical performance. Furthermore, representative cathodes, including manganese-based oxides, vanadium-based compounds, Prussian blue analogues and organic cathode materials, are systematically summarized in terms of structure, performance, and optimization strategies. Finally, the review outlines current challenges and prospective research directions for advancing next-generation high-performance AAIBs cathodes. This review is expected to provide valuable insights for guiding cathode material design and inspire future strategies to enhance the capacity, stability, and rate performance of AAIBs.

Keywords: aqueous aluminum ion batteries, cathode materials, Al^{3+}-cathode interaction, charge storage mechanism, cathode performance

1. Introduction

The fast-growing global energy consumption has intensified the demand for sustainable and efficient energy storage, driving the advancement of next-generation electrochemical storage technologies. In recent decades, lithium-ion batteries (LIBs) have dominated portable electronics, electric vehicles, and grid-scale applications, owing to their high energy density and long cycle life.[1-3] However, their further advancement is hindered by intrinsic limitations: scarce lithium resources increase cost and supply risks, while flammable and toxic organic carbonate electrolytes pose serious safety hazards such as leakage, combustion, and even explosion.[4, 5] Moreover, repeated lithium plating and stripping also induce dendrite formation, which can trigger internal short circuits and thermal runaway.[6-8] These issues highlight the urgent need for the development of next-generation electrochemical storage systems that offer enhanced safety, environmental friendliness,

View Article Online
DOI: 10.1039/D5SC09176D

and cost-effectiveness.

In response to these challenges, researchers have turned attention to post-lithium-ion batteries based on abundant elements such as sodium (Na), potassium (K), zinc (Zn), magnesium (Mg), calcium (Ca), and aluminum (Al).[9-16] Among these, aluminum has attracted particular attention as the most abundant metal in the Earth's crust (~8.2 wt%) and low cost (Figure 1a).[17] Furthermore, aluminum can reversibly transfer three electrons per atom, yielding a high theoretical gravimetric capacity of ~ 2980 mAh g^{-1} and a volumetric capacity of ~ 8046 mAh cm^{-3}, which is approximately four times that of lithium metal.[18] These attributes position aluminum as a promising candidate for the development of high-capacity and cost-effective energy storage systems. Aluminum-ion batteries (AIBs) are typically categorized into two types based on the electrolyte: organic and aqueous systems.[19, 20] Organic AIBs generally utilize ionic liquids as electrolytes, whereas aqueous AIBs (AAIBs) employ aqueous solutions of aluminum salts. Compared to organic systems, aqueous electrolytes offer several advantages, including non-toxicity, low cost, and non-flammability, thereby ensuring enhanced safety and stability.[21, 22] Additionally, their low viscosity and high dielectric constant contribute to high ionic conductivity, improving electrochemical kinetics.[18] Consequently, AAIBs have attracted widespread attention as a safe, low-cost, and high-performance energy storage technology, with a rapidly increasing number of publications in recent decades (Figure 1b).

Nevertheless, AAIBs still face several scientific and technical challenges. Although trivalent Al^{3+} offers a high theoretical capacity, its small ionic radius and high charge density (364 C mm^{-3}) lead to strong electrostatic interactions within the cathode matrix.[18, 23-25] These interactions hinder ion migration and charge transfer, limit the reversible insertion/extraction of Al^{3+}, and induce structural distortion and collapse during cycling, resulting in rapid capacity decay. Additionally, side reactions in aqueous electrolytes, such as hydrogen evolution, anode corrosion, and the formation of passivating oxide layers, further deteriorate Coulombic efficiency and cycling stability.[26, 27] These issues highlight that one of the key directions for advancing AAIBs lies in designing cathode materials capable of regulating Al^{3+}-host interactions to achieve reversible ion storage with minimal structural deformation. A mechanistic understanding of how cathode structure and chemical characteristics govern Al^{3+} accessibility, migration kinetics, and redox reversibility is therefore essential for guiding the rational development of high-capacity, high-rate and high-stability cathode systems. To date, most published reviews on AAIBs have primarily provided general overviews of recent progress and challenges in cathodes, anodes, and electrolytes.[21, 28-30] However, comprehensive reviews dedicated to AAIBs cathode materials remain scarce, and systematic comparisons of their structural characteristics, energy storage mechanisms, and electrochemical behaviors are still lacking.

Therefore, this review presents a systematic analysis of cathode materials for AAIBs. We first outline the fundamental energy storage mechanisms, with particular emphasis on how the chemical nature and structural characteristics of the cathode, along with the electrolyte environment, govern Al^{3+} transport behavior and host–guest interactions, thereby determining the electrochemical performance in terms of capacity, reversibility, rate capability, and cycling stability. Subsequently, we categorize representative cathodes into four categories: manganese-based oxides, vanadium-based compounds, Prussian blue analogues, and organic materials (Figure 2), and discuss their structural features, corresponding electrochemical behaviors and optimization strategies. By comparing their distinct Al^{3+}-host interactions mechanisms and structure-performance relationships,

View Article Online
DOI: 10.1039/D5SC09176D

this review aims to provide a comprehensive scientific guidance for the rational design and future development of high-performance cathode materials for AAIBs. Finally, the challenges and promising research directions for each cathode category are summarized to inspire further progress in this emerging field.

2. Energy storage mechanisms of AAIBs

AAIBs are typically composed of cathode, anode, electrolyte and separator. The cathode materials are primarily transition-metal oxides or organic compounds, while aluminum metal or aluminum alloys serve as the anode. Glass fiber is commonly used as the separator, and the electrolyte usually consists of aqueous solutions containing aluminum salts such as $Al(OTf)_3$ or $Al_2(SO_4)_3$.

During the charge-discharge process, reversible redox reactions occur at both electrodes. The Al^{3+} ions in solvated form (denoted Al^{3+} for simplicity) serve as charge carriers that migrate through the electrolyte, while electrons are transferred in the external circuit between the anode and cathode. Specifically, during discharge, the aluminum anode undergoes oxidation, releasing three electrons to form Al^{3+} (Equation 1). The Al^{3+} ions migrate toward the cathode through the electrolyte, whereas the released electrons travel through the external circuit to reach the cathode. The active cathode material in the oxidation form ($Cathode_{[ox]}$) gains electrons and undergoes transformation into the reduction form ($Cathode_{[red]}$), accompanied by host-guest interaction between the incoming Al^{3+} species and the reduced cathode material (Equation 2). In the subsequent charging process, this reaction reverses: Al^{3+} ions are extracted from the cathode, migrate back to the anode, and are reduced to metallic aluminum, thereby completing a reversible charge-discharge cycle.

$$\text{Anode:}\quad Al - 3e^- \underset{charge}{\overset{discharge}{\rightleftharpoons}} Al^{3+} \tag{1}$$

$$\text{Cathode:}\quad Cathode_{[ox]} + Al^{3+} + 3e^- \underset{charge}{\overset{discharge}{\rightleftharpoons}} Al^{3+}\cdots Cathode_{[red]} \tag{2}$$

$$\text{Overall:}\quad Al + Cathode_{[ox]} \underset{charge}{\overset{discharge}{\rightleftharpoons}} Al^{3+}\cdots Cathode_{[red]} \tag{3}$$

2.1 Factors affecting electrochemical mechanism

The energy storage mechanism of AAIBs is related to the reaction shown in Equation 3, i.e., the host-guest interactions between Al^{3+} and the cathode active species, the reversibility of reaction 3 in the charge-discharge process, and the possible occurrence of side reactions. These factors are ultimately dictated by the structural and chemical characteristics of the cathode material, as well as the electrolyte environment, including the anion salt type, concentration and pH, which in turn determine the key electrochemical performance metrics of AAIBs.

Firstly, the chemical nature of the cathode material is a key factor governing the energy storage mechanism of AAIBs. The type of electroactive centers not only determines the redox reversibility but also influences the type and strength of interaction with Al^{3+}. For inorganic transition-metal oxide cathodes, the specific redox couples control both electron-transfer reversibility and reaction kinetics, depending on the electronic structure of the metal centers. Transition metals with partially filled 3d orbitals enable reversible redox reactions, such as Mn ($Mn^{2+}/Mn^{3+}/Mn^{4+}$) and V ($V^{3+}/V^{4+}/V^{5+}$) oxides. Their tunable valence ranges allow multiple electron transfers with minimal structural distortion, making them the most widely studied inorganic cathode materials.[31-33]

View Article Online
DOI: 10.1039/D5SC09176D

Nevertheless, strong Coulombic interactions between Al^{3+} and oxygen in the metal oxide can induce lattice stress or even structural collapse during repeated Al^{3+} extraction/insertion, thereby limiting the rate capability and cycling stability. For organic cathodes, the redox reversibility primarily depends on the intrinsic reversibility of the functional groups, such as C=O / C–OH. Functional groups within conjugated π-systems or capable of stabilizing negative charges or radical intermediates tend to exhibit higher reversibility.[34, 35] During discharge, Al^{3+} coordinates with these negatively charged sites to maintain charge neutrality, so the stability of Al^{3+}–functional group interaction also dictates the redox reversibility. Compared with inorganic cathodes, organic cathodes exhibit weaker Al^{3+} coordination, leading to less structural distortion during ion transport and consequently superior rate capability and cycling stability.

Secondly, the structural characteristics of the cathode material also affect the energy storage mechanism of AAIBs. Parameters such as interlayer spacing, cavity size, and the exposure of active sites directly determine Al^{3+} accessibility and diffusion kinetics. Cathodes featuring larger interlayer spacing or more open frameworks offer wider migration channels, thereby facilitating faster Al^{3+} transport and enhancing redox reactions during charge and discharge. For inorganic transition-metal oxide cathodes, layered structures generally provide larger diffusion pathways for Al^{3+} compared with tunnel-type frameworks, resulting in improved ion transport kinetics. However, the relatively weak structural rigidity of layered materials makes them prone to lattice strain or even collapse upon repeated Al^{3+} insertion and extraction. Therefore, achieving a balance between sufficient diffusion space and structural stability remains a critical challenge. For organic cathodes, the highly exposed active centers facilitate ion accessibility, while the flexible molecular backbones can effectively accommodate volume changes, thereby mitigating structural stress during cycling. As a result, despite of relatively lower specific capacity, organic cathodes generally exhibit superior structural stability and rate performance compared with rigid inorganic counterparts.

In addition, the electrolyte environment, including anion salt type, concentration and pH, also significantly affects the charge-discharge behavior and energy storage mechanisms of AAIBs. These factors determine the solvation structure of Al^{3+} and the likelihood of side reactions. Typically, in highly concentrated electrolytes, the proportion of free water is reduced. This suppresses water activity, mitigates the hydrogen evolution reaction (HER), and facilitates the reversible deposition of Al on the anode.[36] The type of anion (e.g., Cl^-, OTf^-, SO_4^{2-}) also regulates the coordination environment of Al^{3+}. For instance, $CF_3SO_3^-$ (OTf^-) can reduce the number of water molecules surrounding cation, thereby promoting ion transport and charge transfer, making it a commonly used salt in aqueous batteries.[37] Moreover, the electrolyte pH also influences the insertion behavior of cations. Adjusting the pH allows selective regulation of Al^{3+} and H^+ insertion during the electrochemical process, with H^+ insertion typically occurring under relatively low pH conditions.[38] Sometimes, the introduction of co-solvents such as acetonitrile (AN) and triethyl phosphate (TEP) into a hydrated eutectic Al^{3+} electrolyte can reduce water activity, suppress side reactions like HER and corrosion, and widen the electrochemical stability window, thereby enhancing the stability and reversibility of AAIBs.[39]

2.2 Impact on electrochemical performance

The aforementioned chemical and structural characteristics of the cathode, together with the electrolyte environment, influence the redox behavior and host-guest interactions with Al^{3+}, ultimately affecting the overall electrochemical performance of AAIBs, including capacity

View Article Online
DOI: 10.1039/D5SC09176D

performances and the cycling stability.

The capacity performances, including rate capacities, are fundamentally dictated by the redox activity and ion transport dynamics within the cathodes. The theoretical specific capacity is primarily determined by the number of electrons involved in redox reactions, governed by the valence changes of metal centers in inorganic cathodes and by the number of redox-active functional groups in organic cathodes. The achievable capacity depends on the structural accessibility of Al^{3+} ions and the efficiency of redox reactions. Inorganic cathode materials with larger interlayer spacing or more open frameworks can better accommodate Al^{3+}, providing wider diffusion channels and sufficient storage sites, thereby enabling higher capacity. Generally, layered structures are more favorable for Al^{3+} accommodation than tunnel-type frameworks, leading to superior capacity performance. For organic cathodes, flexible backbones or porous structures can facilitate Al^{3+} diffusion, while densely packed molecules often exhibit lower practical capacities due to limited ion accessibility. The rate capability is largely determined by the diffusion kinetics of Al^{3+} within the cathode and the efficiency of charge transport. Slow ion diffusion limits charge transfer per unit time, resulting in significant capacity decay at high current densities. For inorganic cathodes, constructing materials with high specific surface area and abundant defects can accelerate ion transport and enhance reaction kinetics. Additionally, hybridization with conductive carbon improves electronic conductivity, further supporting high-rate performance. For organic cathodes, highly exposed active sites facilitate rapid Al^{3+} access and diffusion, promoting excellent rate capability.

For the cycling stability, both the intrinsic redox reversibility of the cathode and the strength of Al^{3+}-host interactions play decisive roles. In inorganic metal oxides cathodes, the high charge density of Al^{3+} leads to strong electrostatic interactions with the lattice, which hinders ion diffusion and induce lattice strain, phase transitions, or even partial dissolution, ultimately reducing reaction reversibility and leading to structural collapse and capacity fading. To mitigate this, introducing stabilizing species, such as metal cations or organic molecules, has been shown to weaken these electrostatic interactions and tune the host-guest coupling strength to a moderate level. This strategy effectively buffers volumetric changes, suppresses structural degradation and maintains framework integrity, thereby enhancing both redox reversibility and cycling stability. In contrast, the interactions between Al^{3+} and organic cathodes are generally mild, making the redox reversibility primarily depend on the intrinsic reversibility of the functional groups. Functional groups within conjugated π-systems or capable of stabilizing negative charges or radical intermediates tend to exhibit good reversibility. Moreover, the flexible molecular backbones of organic cathodes can effectively accommodate volumetric changes during Al^{3+} interaction, helping to preserve framework integrity and enhance cycling stability. Additionally, dissolution of cathode materials leads to active material loss and structural degradation, thereby accelerating capacity fading and shortening cycling life.

Collectively, the intrinsic redox behavior of the cathode active centers and the host-guest interactions between Al^{3+} and the cathode material jointly determine the key electrochemical parameters of AAIBs, including specific capacity, rate capability, reversibility, and cycling stability. Therefore, a rational selection of cathode materials and modulation of Al^{3+}-host interactions are of great significance for the design of next-generation high-performance cathode materials for AAIBs.

View Article Online
DOI: 10.1039/D5SC09176D

3. Cathode materials for AAIBs

3.1 Manganese-based cathode material

Manganese oxides have attracted intensive attention as cathode materials for energy storage, primarily due to their abundant natural reserves, low cost and nontoxicity.[31, 40] The multiple oxidation states of manganese ($Mn^{2+}/Mn^{3+}/Mn^{4+}/Mn^{7+}$) support multi-electron transfer reactions, thereby enabling a high theoretical specific capacity of 616 mAh g^{-1} (based on the Mn^{4+}/Mn^{2+} redox couple). In addition, this redox flexibility leads to the formation of a variety of manganese oxides with distinct structures (Figure 3). MnO_2 and Mn_2O_3 are generally composed of edge- or corner-sharing [MnO_6] octahedra, while MnO adopts a face-centered cubic structure, and Mn_3O_4 is considered as a mixture of Mn_2O_3 and MnO.[41, 42] Notably, MnO_2 exhibits diverse phases, including tunnel-type (e.g., α-MnO_2, β-MnO_2, R-MnO_2, T-MnO_2, γ-MnO_2), layered-type (e.g., δ-MnO_2, birnessite) and three-dimensional spinel-type (e.g., ε-MnO_2). This structural diversity endows Mn-based oxides with tunability in Al^{3+} storage behavior, making them highly attractive cathode materials for AAIBs, with ongoing efforts focused on elucidating their intercalation mechanisms and enhancing electrochemical performance through structural engineering.

The electrochemical stability and ion transport properties of manganese oxides are strongly dependent on its crystal structure.[43] Among tunnel-type MnO_2, β-MnO_2 possesses the narrowest channels (1 × 1, 2.3 × 2.3 $Å^2$), and is considered the most thermodynamically stable.[41] However, its narrow tunnels severely limit ion diffusion, resulting in poor electrochemical performance. To date, no studies have reported its application as a cathode in AAIBs. In contrast, α-MnO_2 features larger 2 × 2 (4.6 × 4.6 $Å^2$) tunnels, which facilitate ion transport and accommodate larger ionic species, making it the most widely investigated tunnel-type MnO_2 for AAIBs cathodes. γ-MnO_2 with mixed 1 × 1 (2.3 × 2.3 $Å^2$) and 1 × 2 (2.3 × 4.6 $Å^2$) tunnels, exhibits intermediate structural openness, and some studies have focused on defect engineering to improve its ion diffusion capabilities. Layered-type δ-MnO_2 offers a larger interlayer spacing (~0.7 nm), significantly exceeding the tunnel sizes of other MnO_2. This enhanced ion-accessible volume and facilitates ion intercalation, and has thus attracted considerable interest as a high-capacity cathode material.[44] In the following sections, we will systematically discuss the electrochemical behavior of different manganese oxides in AAIBs.

3.1.1 Tunnel-type manganese oxides

In 2018, Archer et al. used α-MnO_2 with a 2×2 tunnel structure as a cathode material in AAIBs.[45] By pairing α-MnO_2 with an ionic liquid treated aluminum anode (TAl), the TAl/2 M $Al(OTf)_3$/α-MnO_2 full cell demonstrated a high specific capacity of 380 mAh g^{-1} and an average discharge potential of approximately 1.3 V at a current density of 100 mA g^{-1}. During electrochemical cycling, a reversible formation and dissolution of an amorphous layer composed of low-valence manganese oxides occur on the surface of α-MnO_2. This study provided the first compelling evidence for the viability of manganese oxides, particularly α-MnO_2, as high-capacity cathode materials in AAIBs. However, the cell showed limited capacity retention, maintaining a discharge capacity of just 168 mAh g^{-1} after 40 cycles at 100 mA g^{-1}.

Given the intrinsic limitations of pristine α-MnO_2, such as sluggish Al^{3+} transport within the narrow tunnels and structural instability arising from repeated Al^{3+}-cathode interactions, subsequent studies have focused on structural optimization strategies, such as introducing defects and expanding tunnel dimensions, to improve ionic accessibility and electrochemical performance. In 2024, Li et al. developed α-MnO_2 with oxygen vacancies (denoted as O_d-MnO_2) by calcination

View Article Online
DOI: 10.1039/D5SC09176D

under an argon atmosphere, and employed it as a cathode material for AAIBs.[46] The introduction of oxygen vacancies facilitated the opening of microstructure, enhancing electrolyte accessibility and accelerating electrochemical reaction kinetics. As a result, the O_d-MnO_2 cathode exhibited improved rate performance and cycling stability. In 5 M $Al(OTf)_3$ electrolyte, it delivered a discharge plateau at ~1.5 V and a high specific capacity of 480 mAh g^{-1} at a current density of 100 mA g^{-1}. Compared to pristine α-MnO_2, O_d-MnO_2 retained 100 mAh g^{-1} after 180 cycles at 500 mA g^{-1}, whereas the capacity of the α-MnO_2 rapidly decayed within 40 cycles (Figure 4a). This enhancement was attributed to the presence of oxygen vacancies, which provided structural flexibility to accommodate volume changes during cycling, thereby improving stability. Therefore, oxygen vacancies can enhance the electrochemical performance of α-MnO_2 by improving ion/electron transport and increasing structural flexibility, making it an effective strategy for MnO_2 optimization in AAIBs.

γ-MnO_2 features a mixed tunnel structure composed of 1 × 1 and 1 × 2 channels, which are narrower than the tunnels of α-MnO_2 and thus less favorable for Al^{3+} intercalation. To overcome this limitation, γ-MnO_2 enriched with oxygen vacancies (denoted as O_v-MnO_2) was synthesized via annealing under argon atmosphere.[47] The introduction of oxygen vacancies can open the MnO_6 octahedral framework, generating additional ion diffusion pathways and extending the proton diffusion path along the *a-c* plane, thereby enhancing the overall capacity (Figure 4b). In 5 M $Al(OTf)_3$ electrolyte, O_v-MnO_2 delivered a high discharge capacity of 481.9 mAh g^{-1} at 200 mA g^{-1}, and maintained 128.6 mAh g^{-1} after 200 cycles at 0.4 A g^{-1}. To the best of our knowledge, β-MnO_2, which possesses only 1 × 1 tunnel structures, has not yet been explored as a cathode material for AAIBs, likely due to its severely limited channel size that restricts Al^{3+} intercalation.

Overall, the ion storage capacity of tunnel-type MnO_2 is strongly influenced by tunnel size. The narrow tunnels, particularly in β- and γ-MnO_2, limit the intercalation of bulky multivalent ions such as Al^{3+}, while α-MnO_2 shows appreciable Al^{3+} storage capacity. To address the inherent diffusion constraints in these tunnel-structured MnO_2, introducing oxygen vacancies has emerged as an effective strategy to expand ion diffusion pathways and enhance the electrochemical performance of these materials.

3.1.2 Layered-type manganese oxides

Compared to tunnel-type MnO_2, layered δ-MnO_2 exhibits larger interlayer spacing (~ 0.7 nm), providing a more open framework for ion diffusion and storage. This structure enables the accommodation of more Al^{3+} and holds promise for achieving higher specific capacities.

In 2019, Yu et al. employed δ-MnO_2 as the cathode material for AAIBs.[48] During the initial discharge, δ-MnO_2 underwent a conversion reaction, in which Mn^{4+} was reduced and dissolved into the electrolyte as Mn^{2+}. Upon subsequent charging, the dissolved Mn^{2+} was oxidized and combined with Al^{3+} to form an amorphous $Al_xMn_{1-x}O_2$, which then served as the active material for the following charge/discharge cycles (Figure 4c). The resulting TAl/2 M $Al(OTf)_3$/δ-MnO_2 coin cell delivered a capacity of approximately 350 mAh g^{-1} at 100 mA g^{-1}. Moreover, increasing Mn^{2+} concentration in the electrolyte has been shown to facilitate the formation of $Al_xMn_{1-x}O_2$ and mitigate further Mn dissolution. By introducing 0.5 M $MnSO_4$, the modified cell exhibited a significantly enhanced capacity of 554 mAh g^{-1} with a discharge plateau around 1.35 V, and retained 320 mAh g^{-1} after 65 cycles, demonstrating improved cycling stability (Figure 4d). These results highlight the critical role of Mn^{2+} in stabilizing the cathode structure and enhancing the electrochemical performance of δ-MnO_2-based AAIBs. In a separate study, δ-MnO_2 paired with a

View Article Online
DOI: 10.1039/D5SC09176D

Pt-sputtered Al anode in a 5 M $Al(OTf)_3$ electrolyte also delivered a high capacity of 452 mAh g^{-1} at 50 mA g^{-1} without any Mn^{2+} supplementation.[49]

Although the layered δ-MnO_2 possesses a large interlayer spacing favorable for Al^{3+} transport, its poor structural stability leads to rapid capacity decay during cycling. In the initial charge/discharge process, δ-MnO_2 undergoes an irreversible electrochemically induced structural rearrangement with Al^{3+} to form a relatively more stable layered amorphous Al_xMnO_2 phase, which subsequently serves as the active material during cycling and mitigates the excessively strong Al^{3+}–MnO_2 interaction in subsequent cycles.[48, 50] Inspired by this electrochemical conversion, direct pre-intercalation of Al^{3+} has been employed to construct relatively stable layered manganese oxides. For instance, Ran et al. synthesized layered $Al_xMnO_2{\cdot}nH_2O$ cathodes via a modified hydrothermal method, when coupled with an Al-Cu alloy anode in a 2 M $Al(OTf)_3$ electrolyte, deliver an initial discharge capacity of approximately 400 mAh g^{-1} at 500 mA g^{-1}, with 83% capacity retention after 400 cycles.[51]

Similar conversion behavior to layered Al_xMnO_2 during the first charge-discharge process has also been observed in other Mn oxide cathodes. In 2019, Lu et al. reported that Mn_3O_4 could be electrochemically converted into a layered $Al_xMnO_2{\cdot}nH_2O$ structure, resulting in a significant enhancement in capacity.[52] During the initial charging process, a portion of Mn^{3+} in octahedral sites was oxidized to Mn^{4+}, while Mn^{2+} in tetrahedral sites and the remaining Mn^{3+} in octahedral sites dissolved into the electrolyte, triggering the formation of a layered phase. The dissolved Mn species subsequently reassembled along the edges of the layered domains in the $Al(OTf)_3$ electrolyte, forming amorphous regions (Figure 4e). As a result, the obtained $Al_xMnO_2{\cdot}nH_2O$ exhibits a mixed-phase structure and delivers a high discharge capacity of 467 mAh g^{-1} at a current density of 30 mA g^{-1}, with a distinct discharge plateau around 1.2 V and a retained capacity of 272 mAh g^{-1} after 60 cycles. The superior capacity of $Al_xMnO_2{\cdot}nH_2O$ arise from its layered structure, which enables easier Al^{3+} diffusion, and the presence of crystal water, which reduces electrostatic interactions between the Al^{3+} and the host anions. Similarly, in 2020, Yan et al. employed MnO as a precursor, which was electrochemically converted into a layered Al_xMnO_2 phase during the initial charge.[53] The resulting Zn-Al/2 M $Al(OTf)_3$/Al_xMnO_2 coin cell exhibited a high discharge plateau (~1.6 V), a stable reversible capacity (460 mAh g^{-1} after 80 cycles at 100 mA g^{-1}), and excellent rate performance (100 mAh g^{-1} at 3 A g^{-1}). Ex situ XANES and XRD analyses confirmed the reversible Mn^{4+}/Mn^{2+} redox behavior and structural evolution during interaction between Al^{3+} and the host lattice, providing solid evidence for a reversible Al^{3+} storage mechanism in MnO-derived Al_xMnO_2 (Figure 4f-g).

In summary, current studies indicate that manganese oxide materials with layered structures offer advantages over tunnel-type structures by providing more space for Al^{3+} storage. However, these layered phases are often structurally unstable and undergo a transformation into more stable layered Al_xMnO_2 phases during the initial charge/discharge process, facilitated by the pre-incorporation of Al^{3+} within the host lattice. Despite these advancements, no systematic comparisons have been conducted to determine which type of manganese oxide converts more effectively into Al_xMnO_2 and delivers better electrochemical performance. The extent of this transformation, including the degree of interaction between Al^{3+} and the cathode material, as well as the ratio between the newly formed Al_xMnO_2 phase and the residual parent phase, remains

View Article Online
DOI: 10.1039/D5SC09176D

unclear. In addition, the atomic ratio of Al to Mn in the Al_xMnO_2 phase, which could reveal the quantitative level of Al^{3+} participation in the structure, has yet to be clearly established.

3.1.3 Modified manganese oxide composites

The pure-phase δ-MnO_2 itself remains intrinsically unstable and tends to transform into Al_xMnO_2 during the initial cycle. Due to the high charge density of Al^{3+}, strong Coulombic interactions arise between Al^{3+} and the host lattice, leading to sluggish diffusion kinetics and even structural collapse during cycling.[54] The formation of the Al_xMnO_2 phase partially mitigates these effects by alleviating the excessively strong Al^{3+}-MnO_2 interaction in subsequent cycles. However, the resulting Al_xMnO_2 still suffers from gradual capacity decay and poor cycling stability, primarily due to the remaining strong electrostatic interactions between Al^{3+} and the host framework that continues to drive structural degradation over prolonged cycling. To address this, recent studies have explored the incorporation of stabilizing species, including organic molecules and heteroatoms, to further reinforce the structural robustness of δ-MnO_2.

Jiang et al. reported a layered manganese oxide cathode pre-intercalated with benzoquinone-coordinated Al^{3+} (BQ-Al_xMnO_2) (Figure 5a).[55] In this design, organic benzoquinone (BQ) molecules coordinate with Al^{3+} to form BQ-Al^{3+} complexes, which are subsequently introduced between MnO_2 layers. This coordination lowers the effective charge of Al^{3+}, weakening its electrostatic interaction with the host lattice and facilitating reversible Al^{3+}-host intercalation. Simultaneously, the co-intercalation of BQ-Al^{3+} complexes expands the interlayer spacing of MnO_2, further improving ion transport and structural stability. As a result, the BQ-Al_xMnO_2 cathode, paired with a $Zn_{50}Al_{50}$ alloy anode and a mixed electrolyte of 2 M $Al(OTf)_3$ and 0.2 M $Mn(OTf)_2$, exhibited outstanding electrochemical performance. The assembled coin cell delivered a discharge capacity of 300 mAh g^{-1} at a current density of 1 A g^{-1}, and maintained ~99% of its capacity after over 800 cycles, demonstrating both high capacity and cycling stability. In addition to organic molecule intercalation, cation pre-intercalation has also proven effective in stabilizing layered MnO_2 frameworks and enhancing electrochemical kinetics. For instance, Cu^{2+} pre-intercalated δ-MnO_2 synthesized via a simple hydrothermal method exhibited a high discharge capacity of 363.4 mAh g^{-1} at 400 mA g^{-1} and retained 164.5 mAh g^{-1} of its capacity after 300 cycles.[56] The incorporated Cu^{2+} increase the electronegativity of lattice oxygen, moderate the strong electrostatic interaction with Al^{3+} and optimize H^+ adsorption energy, thereby enhancing proton participation and maintaining the layered structure.

Metal cation substitution, especially with aliovalent ions, can simultaneously tailor the host structure and introduce charge carriers (holes or electrons) to maintain charge neutrality, thereby enhancing the structural stability of the cathode material.[57, 58] Building on this concept, Geng et al. developed a defective cobalt-substituted layered manganese oxide (δ-MnO_2) as a cathode material for AAIBs (Figure 5b-c).[59] The synergistic effect between the incorporated Co atoms and Mn vacancies improved the electrical conductivity, facilitated Al^{3+} diffusion, and effectively suppressed Mn dissolution during cycling (Figure 5d). As a result, the assembled battery exhibited a high specific capacity of 585 mAh g^{-1} at a current density of 100 mA g^{-1}, with 78% capacity retention after 300 cycles. However, the Co-doped δ-MnO_2 exhibited relatively poor rate capacity, delivering only 185 mAh g^{-1} at a high current density of 500 mA g^{-1}. To improve this, our group introduced metal heteroatoms with higher metal-oxygen bond dissociation energies, such as V and Ti, to reinforce the δ-MnO_2 framework while expanding the interplanar spacing (Figure 5e-f).[60] The

View Article Online
DOI: 10.1039/D5SC09176D

enlarged interlayer spacing reduces diffusion resistance and accelerates Al^{3+} transport and adsorption, resulting in enhanced rate performance. Meanwhile, the stronger metal-oxygen bonds improve structural stability and suppress Mn dissolution. As a result, the V-doped δ-MnO_2 cathode achieved a high reversible capacity of 518 mAh g^{-1} at 200 mA g^{-1} with 86% capacity retention over 400 cycles. Moreover, its rate performance was significantly improved, delivering 468, 339, and 285 mAh g^{-1} at 0.5, 1, and 2 A g^{-1}, respectively.

Another strategy to enhance the structural stability and electrochemical performance of MnO_2 cathodes is the composite approach. By integrating MnO_2 with other functional materials such as conductive carbon, the resulting hybrid structures can enhance structural stability, suppress manganese dissolution, stabilize oxygen vacancies, or provide additional active sites for ion storage.[32, 61] For instance, a hybrid α-MnO_2 cathode with Al^{3+} pre-insertion and g-C_3N_4 was developed, where Al^{3+} expands the tunnel structures and reduces strain during intercalation, while g-C_3N_4 occupies oxygen vacancies and forms Mn-N bonds with the MnO_6 lattice.[62] This dual modification not only improves structural robustness but also significantly enhances electrochemical performance, delivering an excellent capacity of 329.25 mAh g^{-1} at 0.5 A g^{-1} and a rate capability of 137.67 mAh g^{-1} at 1.5 A g^{-1}, highlighting the effectiveness of composite engineering in stabilizing MnO_2 cathodes for AAIBs.

Overall, tunnel-type MnO_2 cathodes suffer from limited capacity due to their narrow channels, whereas layered δ-MnO_2 offers greater interlayer spacing, making it a more promising host for Al^{3+} storage. However, the layered structure is inherently unstable and typically undergoes an in-situ transformation into a Al_xMnO_2 phase during the initial charge/discharge cycle. In addition to δ-MnO_2, other manganese oxides such as MnO and spinel-type Mn oxides can also be electrochemically converted into Al_xMnO_2 during initial cycling. Nevertheless, the stability of the resulting Al_xMnO_2 remains limited. Therefore, recent research has focused on interlayer engineering strategies, such as organic molecule intercalation, metal-ion pre-intercalation, and heteroatom doping, to stabilize or enlarge the interlayer spacing and suppress structural degradation. These methods aim to preserve the advantageous layered framework while enhancing both the cycling stability and rate performance of Mn-based cathodes. Future research could further refine and integrate these strategies to develop high-performance and durable manganese-based cathode materials for AAIBs.

3.2 Vanadium-based cathode material

Metallic vanadium, with its wide range of oxidation states from +2 to +5, enables multi-electron transfer and thus delivers high capacities, making vanadium-based compounds an important class of cathode materials. Vanadium-based compounds include vanadium oxides, vanadates, and vanadium phosphates. Among them, vanadium oxides are the most widely studied. Owing to the variable oxidation states of vanadium, vanadium oxides exhibit diverse crystal structures, primarily including orthorhombic layered V_2O_5, bilayer $V_2O_5 \cdot nH_2O$, $V_3O_7 \cdot H_2O$, as well as monoclinic tunnel-structured VO_2, V_6O_{13}, and V_2O_3. Vanadates, generally denoted as $M_xV_nO_m$ (where M represents metal cations or ammonium ions), are derived from the pre-intercalation of metal ions into vanadium oxides. Such pre-intercalation is beneficial for enhancing the structural stability of vanadium oxides. Vanadium phosphates are constructed from [PO_4] tetrahedra and [VO_6] octahedra, forming a three-dimensional open framework. They typically exhibit a robust structural framework and remarkable thermal stability, as well as good structural integrity during ion

View Article Online
DOI: 10.1039/D5SC09176D

insertion/extraction. However, the separation of [VO_6] octahedra by phosphate groups leads to intrinsically low electronic conductivity. The variations in crystal structures and chemical compositions among these vanadium-based compounds lead to differences in electrochemical performance, which provides both opportunities and challenges for their application as cathodes in AAIBs.

3.2.1 Vanadium oxides

In 2016, González et al. first employed V_2O_5 as a cathode material for AAIBs and explored the possibility of Al^{3+} intercalation into V_2O_5.[63] Using a three-electrode configuration in 1 M $AlCl_3$ electrolyte, they found that during discharge, V_2O_5 irreversibly transformed into amorphous $Al_xV_2O_5$. The amorphous structure facilitated dynamic chemical interactions with Al^{3+}-containing electrolyte species, thereby enhancing the charge storage capacity.

Subsequently, in 2020, Zhao et al. proposed that in AAIBs, protons can reversibly interact with V_2O_5, whereas direct Al^{3+} participation is difficult.[38] By tuning electrolyte composition and pH, they regulated H^+ intercalation selectivity (Figure 6a). In 2 M $Al(OTf)_3$ acidic electrolyte, V_2O_5 delivered a discharge capacity of ~200 mAh g^{-1} at 20 mA g^{-1}, with a discharge plateau around 0.9 V and 120 mAh g^{-1} remaining after 50 cycles (Figure 6b). DFT calculations revealed that proton insertion induced a structural transformation from orthorhombic layered V_2O_5 to a triclinic phase, accompanied by reductions in both interlayer spacing and volume. The insertion of one proton could deliver ~147 mAh g^{-1} with good structural stability, whereas insertion of two protons increased the capacity to 296 mAh g^{-1} but caused significant volume contraction and severe structural degradation (Figure 6c). These studies clarified the ion storage behavior in V_2O_5, though the dominant mechanism remains under debate.

To enhance the electrochemical performance of V_2O_5, in 2023, De et al. synthesized interconnected nanosheet-structured V_2O_5 via a hydrothermal method using NH_4VO_3 followed by high-temperature calcination.[64] This two-dimensional nanosheet architecture increased the electrode-electrolyte contact area, facilitating rapid ion diffusion. In a three-electrode setup with 0.5 M $AlCl_3$ electrolyte, the electrode delivered an initial discharge capacity of ~140 mAh g^{-1} at 0.5 A g^{-1}, and maintained 96% of its capacity after 1000 cycles at 1 A g^{-1} (Figure 6d). The excellent capacity retention and rate performance were attributed to the high specific surface area provided by the interconnected nanosheet structure, which promoted ion accumulation at the electrode-electrolyte interface, enhancing the electric double-layer contribution to the total capacity.

Introducing oxygen vacancies is another effective strategy. Wang et al. introduced oxygen vacancies (O_v) into V_2O_5 via oxalic acid treatment.[65] The resulting O_v-V_2O_5 exhibited a high initial capacity of 400 mAh g^{-1} at 0.4 A g^{-1} in 5 M $Al(OTf)_3$ electrolyte, nearly double that of pristine V_2O_5 (~200 mAh g^{-1}) (Figure 6e). Theoretical calculations indicated that O_v-V_2O_5 had lower adsorption energies for both H^+ and Al^{3+} compared with pristine V_2O_5, implying reduced diffusion barriers and accelerated ion transport. Although oxygen vacancies improved cycling stability (Figure 6f), the capacity of O_v-V_2O_5 still declined to 103 mAh g^{-1} after 200 cycles, indicating rapid fading.

Besides defect engineering, compositing with conductive materials has also been investigated to improve the electrochemical performance of V_2O_5. Yang et al. fabricated a V_2O_5@MXene composite cathode by depositing rod-like V_2O_5 onto monolayer MXene.[66] In 5 M $Al(OTf)_3$ electrolyte, the composite exhibited a wide voltage window (0.1-2.4 V) and an exceptionally high initial capacity of 626 mAh g^{-1} at 100 mA g^{-1} (Figure 6g). Compared with pristine V_2O_5, the composite demonstrated approximately twice the cycle life, improved coulombic efficiency, and

View Article Online
DOI: 10.1039/D5SC09176D

retained 200 mAh g^{-1} after 100 cycles at 400 mA g^{-1} (Figure 6h). The enhanced performance was attributed to the excellent electrical conductivity and pseudocapacitive characteristics of MXene, which improved electron transport, ion diffusion, and electrode stability.

In summary, layered V_2O_5 enables reversible interactions with Al^{3+} or H^+ in AAIBs but suffers from limited capacity and structural instability. Although defect engineering and conductive composite design have improved capacity and cycle life, the capacity fading remains significant. Therefore, stabilizing the crystal structure and enhancing the reversible ion storage are critical directions for the future development of V_2O_5-based cathodes.

Compared with layered V_2O_5, tunnel-type vanadium oxides generally exhibit higher lattice stability during repeated ion-host interaction, which is beneficial for achieving long cycle life.[67, 68] Among them, the most representative is the metastable monoclinic bronze-type vanadium dioxide (VO_2(B)), whose crystal structure consists of alternating [VO_6] octahedra and tetrahedra, forming characteristic one-dimensional diffusion tunnels. The tunnel size (4.984 Å×3.281 Å) is significantly larger than the ionic radius of Al^{3+} (0.53 Å), thus providing sufficient space for guest ion transport and storage.

Recent studies have further optimized the VO_2 structure to enhance its electrochemical performance in AAIBs. In 2020, Cai et al. synthesized porous VO_2(B) nanobelts via a hydrothermal method and employed them as cathode materials for AAIBs.[69] The robust VO_2(B) framework effectively resisted lattice shear during cycling, while the porous nanobelt morphology shortened ion diffusion pathways and increased electrode-electrolyte contact area. As a result, the electrode delivered a specific capacity of 234 mAh g^{-1} at 150 mA g^{-1} and retained 77.2% of its capacity after 1000 cycles at 1 A g^{-1} in a three-electrode system with 5 M $Al(OTf)_3$ electrolyte (Figure 7a-b). In another study, Wang et al. reported that the unique interconnected tunnel structure of monoclinic VO_2 enabled rapid Al^{3+} diffusion while effectively mitigating volume changes, achieving 235 mAh g^{-1} at 200 mA g^{-1}, and retaining 49.3% of its capacity when the current density increased to 2 A g^{-1} (Figure 7c).[70]

More recently, in 2025, Wang et al. achieved both a compositional transformation from V_2O_5 to VO_2 and a crystallographic transition from the orthorhombic to the monoclinic phase via glucose-assisted hydrothermal reduction, while simultaneously introducing Cu^{2+} doping (Figure 7d).[71] The introduced Cu 3d orbitals enhanced the hybridization between V 3d and O 2p orbitals and strengthened electronic coupling, optimizing the band structure and improving both ion and electron transport. At an optimal Cu content of 1 mmol, the resulting VO_2 cathode, paired with 5 M $Al(OTf)_3$ electrolyte and ionic-liquid-treated Al anode, delivered an initial discharge capacity of 642 mAh g^{-1} at 0.4 A g^{-1} and maintained 116 mAh g^{-1} after 200 cycles at 0.8 A g^{-1} (Figure 7e-f), outperforming pristine VO_2 in both capacity and cycling stability.

In summary, VO_2(B) demonstrates considerable potential for AAIBs applications owing to its spacious tunnel structure. However, unlike layered vanadium oxides, where interlayer spacing can be tuned to enhance ion diffusion kinetics, the tunnel dimensions of VO_2 are relatively fixed, restricting further improvement in ion diffusion kinetics. Therefore, effective strategies to accelerate ion migration within the tunnels are urgently needed. Current strategies, including nanostructure design to shorten diffusion paths and doping to optimize electronic structure, have enhanced performance. Nevertheless, there remains substantial room for improvement in their long-term cycling stability and high-rate capability.

View Article Online
DOI: 10.1039/D5SC09176D

3.2.2 Vanadates

Due to the flexible distortion of V-O polyhedra and the multiple oxidation states of vanadium, V-O frameworks exhibit high structural adaptability toward the incorporation of foreign metal cations and ammonium ions, giving rise to a wide variety of vanadates. These materials can be regarded as derivatives formed by the combination of vanadium oxides with additional ions or clusters. Typically, the introduced cations act as "pillars" within the framework, enhancing interlayer stability and improving ion transport kinetics, thereby boosting electrochemical performance.

In 2022, Soundharrajan et al. reported the application of LiV_3O_8 cathodes in AAIBs.[72] The presence of Li^+ in its layered structure can mitigate the strong Coulombic attraction between Al^{3+} and the host lattice, thereby facilitating Al^{3+} diffusion kinetics (Figure 8a). In 2 M $Al(OTf)_3$ electrolyte, LiV_3O_8 delivered a high capacity of 289 mAh g^{-1} at 0.29 C and maintained 147 mAh g^{-1} after 500 cycles at 0.59 C, corresponding to a capacity retention of 77.3% (Figure 8b-c).

In 2023, Liu et al. for the first time applied $NH_4V_4O_{10}$ as a cathode for AAIBs.[73] The large and lightweight NH_4^+ act as pillars in the crystal structure, expanding the interlayer spacing and promoting fast ion transport. As a result, the layered $NH_4V_4O_{10}$ achieved 257.78 mAh g^{-1} at 0.5 A g^{-1} in 2 M $Al(OTf)_3$, and retained 87.80 mAh g^{-1} even at a high current density of 5 A g^{-1} (Figure 8d). Subsequent work further examined electrolyte optimization for $NH_4V_4O_{10}$ cathode material. Priya H et al. demonstrated that adding 0.5 M NH_4Cl to 1 M $AlCl_3$ electrolyte effectively suppressed vanadium dissolution.[74] The first-cycle capacity decay decreased from 84% to 32%, and the electrolyte color changed from deep yellow to light yellow (Figure 8e-f), indicating that the additive suppressed V dissolution and improved structural stability.

In addition, Wu et al. prepared $(NH_4)_2V_{10}O_{25}\cdot 8H_2O/Ti_3C_2T_x$ composites via van der Waals self-assembly.[75] The incorporation of MXene reduced the charge-transfer resistance to one-tenth that of pristine material and significantly enhanced both rate capability and cycling stability (Figure 8g-h). At 1.0 A g^{-1}, the electrode maintained 268.7 mAh g^{-1} after 110 cycles (Figure 8i). This result indicates that MXene not only accelerates ion transport but also acts as a mechanical support to stabilize structure during cycling, highlighting the advantages of composite design.

3.2.3 Vanadium phosphates

Vanadium phosphates are composed of $[VO_6]$ octahedra and $[PO_4]$ tetrahedra, forming a three-dimensional open framework with excellent crystallographic stability and can maintain structural integrity during cycling. The presence of $[PO_4]$ tetrahedra introduces a P-O covalency-induced effect, which weakens the V-O covalent bonds, thereby endowing vanadium phosphates with relatively high redox potentials.[76] However, similar to other phosphate-based electrodes, the $[VO_6]$ octahedra are isolated from each other by intervening $[PO_4]$ tetrahedra, which hinders electron transport pathways and results in intrinsically low electrical conductivity.[77]

In 2018, Nacimiento et al. first applied NASICON-type $Na_3V_2(PO_4)_3$ as a cathode for rechargeable aluminum batteries, delivering a reversible capacity of 60-100 mAh g^{-1} at current densities ranging from 10 to 1000 mA g^{-1} in a three-electrode configuration with $AlCl_3$-based electrolyte (Figure 9a).[78] In 2020, Wang et al. employed $VOPO_4$ as the cathode and incorporated a mechanically robust gelatin-polyacrylamide hydrogel electrolyte to construct a flexible AAIBs, achieving a capacity of 88 mAh g^{-1} at 0.8 A g^{-1} and maintaining 22 mAh g^{-1} even at a high rate of 6 A g^{-1} (Figure 9b).[79] Remarkably, this device retained 86.2% of its initial capacity after 2800 cycles

at 1 A g^{-1} (Figure 9c), demonstrating excellent cycling stability and mechanical flexibility. Subsequently, Pang et al. utilized layered $VOPO_4 \cdot 2H_2O$ nanosheets as a cathode material for AAIBs, achieving reversible trivalent Al^{3+} storage in 2.5 M $Al(OTf)_3$ electrolyte.[80] At a current density of 20 mA g^{-1}, the material delivered an initial discharge capacity of 125.4 mAh g^{-1} with an operating voltage of ~0.9 V, retaining 60% of its capacity after 40 cycles (Figure 9d-e), highlighting its cycling stability and application potential. More recently, Liu et al. demonstrated that phenylamine intercalation can effectively expands the interlayer spacing of $VOPO_4$, enabling high-capacity and long-life Al^{3+} storage in aqueous batteries.[81]

Overall, the capacities and operating voltages of vanadium-based cathodes in AAIBs are generally lower than those of manganese-based counterparts, primarily due to their intrinsic structural and electronic limitations, including relatively low electrical conductivity and suboptimal ion transport pathways. Future research should focus on improving the capacity, stability, and conductivity through strategies such as nanostructure engineering, conductive network construction, and doping modifications, while combining *in situ* characterizations with theoretical calculations to gain deeper insights into their energy storage mechanisms.

3.3 Prussian blue analogs

Prussian blue analogs (PBAs) were first discovered in the 18th century and widely employed as dyes. It was not until 2011 that Cui et al. first utilized KNi-PB as a cathode material for potassium-ion batteries, followed by their report on the application of KCu-PB in lithium-ion batteries.[82, 83] These pioneering studies not only broadened the application scope of PBAs in rechargeable ion batteries but also revealed their great potential as cathode materials.

PBAs are generally represented by the formula $A_xM[M'(CN)_6]_{1-y} \cdot \square_y \cdot nH_2O$ ($0 < x < 2$), where A denotes alkali metal ions (commonly K, Na, or Li), M corresponds to N-coordinated transition metal ions, M' refers to C-coordinated transition metal ions (most commonly Fe), and □ represents vacancies arising from the loss of $M'(CN)_6$ units and the occupation by coordination water.[84, 85] Prussian blue and its analogues are often abbreviated as AM-PB. In AM-PB, the Fe^{2+}/Fe^{3+} redox couple at the M' site generally serves as the dominant redox pair. When the M-site metal is also electrochemically active (e.g., Fe, Co, Mn), an additional M^{2+}/M^{3+} redox couple is introduced, enabling two redox-active centers and thus a higher theoretical capacity. In contrast, when M is electrochemically inactive (e.g., Ni, Cu, Zn), only the Fe^{2+}/Fe^{3+} redox couple contributes to charge storage, resulting in a lower theoretical capacity.[86]

The ideal PBA structure adopts a face-centered cubic framework with a lattice parameter of ~10.2 Å (Figure 10a). In this structure, C≡N groups are located along the cube edges, where M and M' ions form octahedral coordination with N and C atoms of cyanide ligands respectively, constructing a three-dimensional open framework. The interstitial sites between octahedra create diffusion pathways for ion transport, thereby allowing the reversible transport and storage of cations. The crystal structure of PBAs can transform among cubic, monoclinic, rhombohedral, trigonal, and tetragonal phases (Figure 10) depending on the A^+ content and the amount of crystalline water.[87, 88] Such structural evolutions significantly influence their electrochemical stability. Moreover, PBAs commonly contain $[Fe(CN)_6]$ vacancies, which are often occupied by coordinated water molecules

View Article Online
DOI: 10.1039/D5SC09176D

(Figure 10f). These vacancies not only reduce the number of active sites but may also disrupt the continuity of the Fe-CN-M framework, leading to structural distortion or collapse and, consequently, inferior cycling performance. Owing to PBAs open three-dimensional framework, facile synthesis, abundant resources, and tunable operating voltage, PBAs have attracted widespread attention as promising electrode materials for energy storage applications.

3.3.1 PBAs with single redox-active center

In 2015, Li et al. synthesized $K_{0.02}Cu[Fe(CN)_6]_{0.7}\cdot 3.7H_2O$ (abbreviated as CuFe-PBA) via a co-precipitation method, and for the first time, demonstrated the reversible Al^{3+} storage in PBAs.[89] In a three-electrode configuration with 1 M $Al(NO_3)_3$ electrolyte, the Al^{3+} intercalated Al_xCuFe-PBA, similar to the Al_xMnO_2 phase observed in Mn-based systems, was employed as the working electrode with activated carbon as the counter electrode, delivering a reversible capacity of ~50 mAh g^{-1} at 1 C, and retaining ~90% of its initial capacity after 1000 cycles at 5 C (Figure 11a). Comparative analysis with other cation systems revealed that the achievable capacity was mainly limited by the number of electron transfers in the Fe^{2+}/Fe^{3+} redox couple, rather than the nature of the inserted cations. This study provided the first clear evidence for the feasibility of reversible Al^{3+} intercalation in PBAs, laying the foundation for subsequent research. Subsequently, Liu et al. employed copper hexacyanoferrate ($KCu[Fe(CN)_6]\cdot 8H_2O$, CuHCF) nanoparticles as cathodes in AAIBs, and elucidated a two-step kinetic mechanism for Al^{3+} intercalation.[90] Cyclic voltammetry revealed two distinct redox peaks, suggesting that Al^{3+} undergoes partial desolvation prior to insertion into the A-site of the framework, a phenomenon attributed to the strong solvation effect of the highly charged Al^{3+} and the necessary desolvation process (Figure 11b). During cycling, Fe^{3+} coordinated to C atom was reduced to Fe^{2+}, while Cu^{2+} coordinated to N atom remained electrochemically inert, serving only to maintain the structural stability. In a three-electrode configuration with 0.5 M $Al_2(SO_4)_3$ electrolyte, CuHCF delivered a discharge capacity of 62.9 mAh g^{-1} at 50 mA g^{-1}, and still retained 46.9 mAh g^{-1} at 400 mA g^{-1}, demonstrating excellent rate performance (Figure 11c). After 1000 cycles at 400 mA g^{-1}, a capacity retention of 54.9% was achieved, with nearly 100% Coulombic efficiency, indicating high utilization and limited side reactions. Nevertheless, the capacity fading was mainly attributed to the dissolution of CuHCF in the acidic $Al_2(SO_4)_3$ electrolyte.

To address the issues of low capacity, short cycle life, and dissolution of CuHCF in aqueous electrolytes, Zhao et al. proposed an electrolyte-engineering strategy by introducing $[Fe(CN)_6]^{3-}$ into the electrolyte to drive the re-nucleation of dissolved transition metal ions, thereby preventing framework degradation (Figure 11d).[91] In the optimized electrolyte, no Cu^{2+} were detected, confirming the effectiveness of this approach. Remarkably, CuHCF delivered ultra-stable electrochemical performance, achieving 99.8% capacity retention after 40,000 cycles at 1 A g^{-1} in 1 M $(NH_4)_2SO_4$ electrolyte with 5 mmol $K_3Fe(CN)_6$ added (Figure 11e). This approach effectively suppressed transition-metal dissolution and enabled ultralong cycling stability of CuHCF. Radhakantha et al. demonstrated that higher electrolyte concentrations can enhance the structural stability of the CuHCF framework, exhibiting near-zero lattice strain during Al^{3+} insertion.[92]

In addition, Zheng et al. investigated the pre-intercalation of Al^{3+} into CuHCF at different temperatures, and found that the sample treated at 40 °C (CuHCF-P40) exhibited the highest capacity and the best cycling performance.[93] CuHCF-P40 delivered a discharge capacity of 83.1 mAh g^{-1} at 50 mA g^{-1}, ~1.6 times higher than pristine CuHCF (Figure 11f). Even after 5000 cycles

at 1000 mA g^{-1}, a capacity of 54.5 mAh g^{-1} was retained, corresponding to 80.3% capacity retention (Figure 11g). This result suggested that moderate Al^{3+} pre-intercalation expands ion transport channels and mitigates structural distortion during cycling, enhancing both capacity and stability, whereas excessive or insufficient Al^{3+} respectively blocks diffusion pathways or fails to stabilize the framework effectively. Building upon this, Sayeed et al. fabricated flexible full cells pairing Al^{3+} pre-intercalated CuHCF cathodes with MoO_3 anodes in a PVA-based 3 M $AlCl_3$ gel electrolyte.[94] The device delivered a 48 mAh g^{-1} at a high current density of 3 A g^{-1}, with negligible capacity fading over 150 cycles. This work not only further validated the effectiveness of Al^{3+} pre-intercalation but also demonstrated its potential for stable and efficient energy storage in flexible and wearable electronic devices.

3.3.2 PBAs with dual redox-active centers

The aforementioned CuHCF-based PBAs cathodes rely solely on the $[Fe(CN)_6]^{4-}/[Fe(CN)_6]^{3-}$ redox couple, and their reversible capacity is therefore inherently limited. To overcome this constraint, in 2019 Zhou et al. synthesized $K_{0.2}Fe[Fe(CN)_6]_{0.79}\cdot 2.1H_2O$ (denoted as FF-PBA), featuring dual transition-metal redox sites, where Fe^{2+} coordinated to N atoms and Fe^{3+} coordinated to C atoms are both electrochemically active.[95] This dual activity was confirmed by the appearance of two well-defined redox peak pairs in the cyclic voltammetry (Figure 12a). In a three-electrode system with a highly concentrated 5 M $Al(CF_3SO_3)_3$ water-in-salt electrolyte (Al-WISE), FF-PBA delivered an initial discharge capacity of 116 mAh g^{-1} and exhibited an average capacity fading rate of only ~0.39% per cycle (Figure 12b). Notably, electrolyte color changes provided visual evidence of dissolution behavior: in 1 M $Al(NO_3)_3$ and 0.5 M $Al_2(SO_4)_3$ solutions, the electrolytes gradually turned light or deep blue, indicating dissolution of FF-PBA. In contrast, the Al-WISE electrolyte showed almost no visible color change even after 50 cycles (Figure 12c), demonstrating that high-concentration electrolytes effectively suppressed dissolution, thereby ensuring long-term cycling stability. Building upon this, Bai et al. assembled a full cell pairing FF-PBA cathode with a deep eutectic-modified Al anode in $Al(OTf)_3$ electrolyte, which delivered a capacity of 85 mAh g^{-1} at 100 mA g^{-1}, and remained at 58 mAh g^{-1} after 150 cycles, with an average Coulombic efficiency of 97.1% (Figure 12d).[96]

Beyond Fe-Fe PBAs, other bimetallic redox-site PBAs (e.g., V-Fe, Mn-Fe, and Co-Fe) have been investigated to enhance the capacity and cycling stability. Gao et al. reported potassium nickel hexacyanoferrate (KNHCF) as a cathode paired with an Al foil anode in 5 M $Al(CF_3SO_3)_3$ electrolyte, revealing for the first time the charge-compensation mechanism of PBAs in multi-metal redox systems.[97] The coin cell achieved an initial discharge capacity of 46.5 mAh g^{-1} at 20 mA g^{-1}. During cycling, Ni gradually dissolved while Fe redox activity increased, compensating for the capacity loss and sustaining overall performance (Figure 12e). Furthermore, owing to the multiple valence states of vanadium, vanadium-based PBAs (V-PBAs) can undergo multi-electron redox processes, thereby providing more active sites for charge storage. Feng et al. synthesized V-PBAs via an acid-assisted hydrothermal method, and the synergistic effect between V and Fe redox centers was found to significantly enhance capacity.[98] In a full cell with Zn anode and a deep eutectic electrolyte (denoted AU15, composed of $Al_2(SO_4)_3$, urea, and H_2O), V-PBAs delivered a high capacity of 161.37 mAh g^{-1} at 0.1 A g^{-1} and maintained ~100 mAh g^{-1} after 500 cycles at 0.5 A g^{-1} (Figure 12f-g), demonstrating excellent capacity retention and cycling stability.

View Article Online
DOI: 10.1039/D5SC09176D

3.3.3 Optimization Strategies for PBAs

Although the introduction of electrochemically active metals such as Mn and Co can significantly enhance the specific capacity of PBAs, the accompanying volume effects inevitably lead to lattice distortion and cycling degradation. To address these challenges, researchers have explored strategies such as defect engineering, entropy engineering, and nanostructure engineering to optimize the overall performance of PBAs.

3.3.3.1 Defect engineering

Introducing defects or vacancies into the PBA framework can broaden the diffusion channels for Al^{3+} transport and improve ionic kinetics, thereby enhancing the electrochemical performance. In 2021, Wang et al. designed a defective manganese hexacyanoferrate (MnFe-PBA) cathode containing $[Fe(CN)_6]$ vacancies, which effectively expanded the Al^{3+} transport pathways and weakened the Coulombic interactions between Al^{3+} and the host framework (Figure 13a-b).[99] Benefiting from this structural feature and the presence of dual electrochemically active sites (Mn^{3+}/Mn^{2+} and Fe^{3+}/Fe^{2+}), the defective MnFe-PBA delivered an initial discharge capacity of 106.3 mAh g^{-1} at 0.2 A g^{-1}, and maintained higher capacity at 1.0 A·g^{-1}. In contrast, the vacancy-free MnFe-PBA-0 exhibited much lower capacity, highlighting the critical role of vacancies in improving both capacity and rate performance (Figure 13c).

Similarly, Shang et al. utilized the strong chelating effect of Na_2EDTA to introduce a controlled number of Mn cation vacancies (V_{Mn}) into the Mn-PBA framework, obtaining V_{Mn}-PBAs.[100] Compared with conventional Mn-PBAs, V_{Mn}-PBAs delivered an initial discharge capacity of 108 mAh g^{-1} at 0.1 A g^{-1}, and consistently outperformed at higher current densities (0.1 - 1.0 A g^{-1}). At 1.0 A g^{-1}, V_{Mn}-PBAs retained 67.4% of capacity after 5000 cycles, in sharp contrast to 26.6% retention for Mn-PBAs (Figure 13d-e). This improvement was attributed to the introduction of vacancies, which effectively suppressed structural deformation and alleviated the unfavorable Jahn-Teller distortion in Mn-N octahedral. As a result, vacancy engineering both enhanced discharge capacity and cycling stability.

3.3.3.2 Entropy regulation

Increasing system entropy (ΔS) can reduce the Gibbs free energy (ΔG), enhancing structural stability and improving redox activity, thereby leading to better electrochemical performance. Liu et al. adopted an entropy-production strategy to design structurally reinforced medium-entropy PBAs (ME-PBAs) frameworks containing multiple redox-active metal, with the composition $Na_{1.69}Mn_{0.34}Co_{0.33}Ni_{0.13}Cu_{0.20}[Fe(CN)_6]_{0.93}\cdot 2.51H_2O$.[101] Compared with single-phase PBAs, ME-PBAs exhibited higher discharge capacities across 0.05 - 1.0 A·g^{-1} and ultra-long cycling stability, retaining 66.9% capacity after 10,000 cycles at 1.0 A g^{-1} (Figure 13f-g). In a full cell with a MoO anode, ME-PBAs delivered 60.9 mAh g^{-1} at 0.5 A g^{-1} and maintained 89.7% of capacity after 600 cycles. This superior performance was attributed to the synergistic contribution of multiple redox centers: Mn and Fe boost capacity, Co and Cu increase operating voltage, and Ni improves long-term stability, collectively enabling higher capacities and faster kinetics.

Du et al. further employed high-entropy PBAs (HE-PBAs) as cathodes for AAIBs.[102] By introducing multiple transition metal, the intrinsic *d*-band (ε_d) of individual metals was broadened and the electronic degeneracy reduced, thereby improving electron-transfer efficiency and accelerating local charge compensation. Benefiting from the long-range disorder and strong lattice strain fields inherent in high-entropy structures, HE-PBAs accommodated lattice breathing effects

View Article Online
DOI: 10.1039/D5SC09176D

while minimizing volume fluctuations during cycling. As a result, HE-PBAs outperformed bimetallic PBAs in both capacity and cycling stability, achieving a remarkable 91.2% capacity retention after 10,000 cycles at a high current density of 5.0 A g^{-1} (Figure 13h).

3.3.3.3 Nanostructure engineering

PBAs with disordered dispersed morphologies often suffer from long ion-transport pathways and insufficient utilization of electrochemically active sites, which limit their overall electrochemical performance. Nanostructure engineering provides an effective means of regulating ion diffusion and structural stability, thereby improving capacity, rate capability, and cycling stability.

In 2020, Ru et al. synthesized potassium cobalt hexacyanoferrate ($K_2CoFe(CN)_6$) nanocube assemblies via a facile hydrothermal method followed by low-temperature calcination, forming a structure reminiscent of the traditional Chinese Burr puzzle framework (Figure 14a).[103] In 1 M $Al(NO_3)_3$ electrolyte, the material retained 76% of its initial capacity after 1600 cycles at 0.1 A g^{-1}. Zheng et al. prepared one-dimensional Co-PBA (1D-CoPBA) via *in situ* reduction with hydrazine hydrate (Figure 14b).[104] The 1D architecture significantly improved electrical conductivity and hydrophilicity, thereby enhancing electrolyte accessibility. As a result, 1D-CoPBA delivered 100.1 mAh g^{-1} at 50 mA g^{-1}, and retained 87% of its capacity after 2000 cycles at 1000 mA g^{-1}, outperforming conventional Co-PBA. Chang et al. employed tannic acid (TA) etching and cation exchange to synthesize Mg-substituted double-walled Mn-PBA nanocubes (MgMn-PBA DWNCs) (Figure 14c).[105] Mg substitution and Mn vacancies provided abundant active sites, buffered volume changes, and improved ion diffusion. Consequently, MgMn-PBA DWNCs delivered a high capacity of 148 mAh g^{-1} with 99.5% retention after 2000 cycles at 1 A g^{-1}, and maintained 74 mAh g^{-1} even at 4 A g^{-1}. Furthermore, a full cell assembled with α-MoO_3 anode exhibited 78.6 mAh g^{-1} after 2000 cycles at 1 A g^{-1}, with an average Coulombic efficiency of 98.5%, demonstrating outstanding Al^{3+} storage capability.

The intrinsic low conductivity of PBAs remains a bottleneck, prompting the development of nanocomposites that combine complementary materials to improve electron transport and overall performance. Zhao et al. fabricated Fe-Co PBA/rGO composites via *in situ* synthesis method (Figure 14d).[106] Owing to the interfacial chemical coupling between Fe-Co PBA and rGO, the composite exhibited enhanced electronic structure and accelerated charge transfer. Compared with pristine Fe-Co PBA, physically mixed Fe-Co PBA/rGO, and rGO, the Fe-Co PBA/rGO composite cathode demonstrated markedly improved rate capability and long-term cycling stability, achieving 112.5 mAh g^{-1} at 0.1 A g^{-1} and maintaining 66.7 mAh g^{-1} after 1500 cycles at 1 A g^{-1}.

In summary, PBAs with their three-dimensional open framework and tunable redox potential, hold great promise as cathode materials for AAIBs. However, their relatively limited capacity and structural instability arising from lattice distortion during cycling remain key bottlenecks. To address these issues, defect engineering enhances ion diffusion, entropy engineering introduces multiple redox-active centers and reinforces structural robustness, and nanostructure engineering shortens diffusion pathways and buffers volume change. These strategies have collectively improved capacity, rate capability and cycling stability. Looking forward, achieving both high capacity and long lifespan while maintaining framework integrity will be crucial for advancing PBAs in AAIBs. The synergistic optimization of defect regulation, entropy modulation, and

View Article Online
DOI: 10.1039/D5SC09176D

nanostructure design, coupled with in-depth mechanistic understanding via *in situ* characterizations and theoretical modeling, is expected to drive PBAs toward next-generation high-performance cathodes.

3.4 Organic Cathode Materials

In recent years, organic cathode materials have attracted extensive attention due to their abundance, environmental friendliness, structural tunability, and facile synthesis. Compared with inorganic metal oxides, organic materials are composed of common elements (C, H, O, N) and possess flexible molecular backbones that can be rationally tailored to optimize electrochemical performance.[107, 108] Furthermore, their intrinsic structural flexibility helps mitigate volume strain during charge/discharge processes, thereby enhancing cycling stability. In addition, the relatively weak coordination or ion-dipole interactions within organic frameworks facilitate the rapid migration of Al^{3+}, avoiding strong electrostatic interactions typically observed in inorganic cathode materials with high Al^{3+} charge density.[109-111]

In terms of energy storage mechanisms, the electrochemical behavior of organic cathodes mainly relies on reversible redox-active groups. Through electron transfer involving carbonyl groups, nitrogen heterocycles, conjugated π frameworks, or radical sites, organic cathodes enable reversible storage and release of Al^{3+}. Based on the type of redox-active center, organic cathode materials can be classified into quinone-based compounds, N-heteroaromatic compounds, conductive polymers, and radical polymers.

3.4.1 Quinone-based compounds

Quinone-based compounds represent one of the most extensively studied classes of organic cathodes owing to their high redox activity and excellent stability in aqueous environments. Their electrochemical activity originates from reversible carbonyl (C=O) redox centers within the molecular backbone, where each C=O group participates in a one-electron transfer, enabling high theoretical capacities. In AAIBs, these carbonyl groups can coordinate with Al^{3+} to store and release charge.

In 2021, He et al. reported tetrachloro-1,4-benzoquinone (TCQ) as a cathode material for AAIBs.[112] TCQ contains two carbonyl groups that serve as redox-active sites for Al^{3+} storage, undergoing a reversible transformation between carbonyl and hydroxyl groups. During discharge, TCQ is reduced to tetrachlorohydroquinone (TCHQ) by accepting two electrons, and the coordinated Al^{3+} substitutes the hydrogen atoms of the hydroxyl groups, while in the charging process Al^{3+} is released and TCHQ is oxidized back to TCQ (Figure 15a). The Al//TCQ full cell with 1 M $Al(OTf)_3$ electrolyte, delivered a specific capacity of 147.7 mAh g^{-1}at 0.2 A g^{-1}, and retained 70.7% capacity after 200 cycles at 2 A g^{-1} (Figure 15b-c), demonstrating good cycling stability. This study provided a solid proof-of-concept for quinone derivatives as stable organic cathodes in AAIBs.

Li et al. further systematically evaluated six representative quinone compounds, namely 1,4-naphthoquinone (1,4-NQ), 1,2-naphthoquinone (1,2-NQ), anthraquinone (9,10-AQ), phenanthrenequinone (9,10-PQ), pyrene-4,5,9,10-tetraone (PTO), and macrocyclic calix[4]quinone (C4Q), in coin-cell configurations (Figure 15d).[113] Among them, C4Q exhibited superior performance due to its large cavity and eight adjacent carbonyl groups, each serving as a redox-active site. As a result, C4Q delivered a higher discharge voltage almost up to 1 V and a specific

View Article Online
DOI: 10.1039/D5SC09176D

capacity of 400 mAh g^{-1} at 40 mA g^{-1} (Figure 15e-f), along with excellent rate capability (300 mAh g^{-1} at 800 mA g^{-1}), good cycling stability (81% capacity retention after 50 cycles), and outstanding low-temperature performance (224 mAh g^{-1} at -20 °C). The pouch-type Al-C4Q cell achieved an energy density of 93 Wh kg^{-1}, highlighting the potential of quinone-based materials for practical AAIBs applications.

3.4.2 N-heteroaromatic compounds

Compounds containing nitrogen atoms within heteroaromatic frameworks, particularly those with C=N imine groups, represent a versatile class of organic cathodes for AAIBs. The C=N groups act as redox-active centers that reversibly convert to -C-N- during discharge while interacting with Al^{3+}. Their extended π-conjugated frameworks and flexible molecular structures provide abundant active sites, offering high theoretical capacities, analogous to carbonyl-based organic cathodes.

In 2021, Chen et al. demonstrated that phenazine (PZ) utilizes its C=N groups as redox-active centers, undergoing reversible -C=N-/-C-N- transformations during Al^{3+} insertion/extraction in 5 M $Al(OTf)_3$ electrolyte.[114] The PZ cathode delivered a high specific capacity of 132 mAh g^{-1} at 50 mA g^{-1}, and retained 76.5% of its capacity after 300 cycles (Figure 15g-h). The excellent cycling stability was attributed to minimal structural changes, extensive π-conjugation, and intrinsic molecular flexibility of PZ, which maintain structural integrity during cycling.

However, small-molecule N-heteroaromatic electrodes often suffer from limited electronic conductivity and partial solubility in aqueous electrolytes, compromising long-term performance.[115] To address these limitations, Li et al. designed dipyrido[3,2-a:2′,3′-c]phenazine-11-carbonitrile (DPPZ-CN), a multifunctional small-molecule cathode incorporating pyridine, pyrazine, and cyano groups (Figure 15i).[116] The highly conjugated N-heteroaromatic backbone enhances π-π stacking and hydrogen bonding, while the electron-withdrawing cyano group modulates electronic delocalization, improving conductivity and increasing working voltage. DPPZ-CN exhibited 211.9 mAh g^{-1} at 100 mA g^{-1} with a voltage plateau of 0.62 V, and retained 117.7 mAh g^{-1} after 1000 cycles at 1 A g^{-1}, corresponding to a capacity retention of 82.4% (Figure 15j-k). Building on this strategy, Lu et al. synthesized diquinoxalino[2,3-a:2′,3′-c]phenazine-2,3,8,9,14,15-hexacarbonitrile (DQP-6CN) functionalized with six cyano groups.[117] The introduction of multiple cyano groups not only increased the number of redox-active sites but also strengthened π-conjugation and reduced local electron density, thus enhancing capacity, electronic conductivity and structural stability. In 5 M $Al(OTf)_3$ electrolyte, DQP-6CN delivered a high reversible capacity of 279 mAh g^{-1} at 400 mA g^{-1}, surpassing that of unsubstituted DQP (193.5 mAh g^{-1}) (Figure 15l). Cyclic voltammetry (CV) revealed multiple distinct redox peaks for DQP-6CN, confirming the simultaneous participation of imine and cyano groups in the redox processes (Figure 15m). Despite these advances, N-heteroaromatic cathodes generally operate at discharge voltages below 0.8 V, lower than quinone-based materials, which remains a limitation for broader applications in AAIBs.

3.4.3 π-conjugated carbonyl-imine hybrid compound

Beyond organic cathodes containing a single type of redox-active center, such as carbonyl or imine groups, recent efforts have focused on constructing hybrid systems that integrate both functionalities within a conjugated backbone. Introducing C=O and C=N groups into a planar π-conjugated framework enables multiple redox-active sites and enhanced intermolecular interactions.

View Article Online
DOI: 10.1039/D5SC09176D

The carbonyl and imine groups both provide reversible electron-transfer centers, increasing theoretical capacity, while the extended π-conjugation improves electronic conductivity, suppresses dissolution, and enhances structural stability. Consequently, π-conjugated carbonyl-imine hybrid compounds have emerged as a promising design strategy for high-performance organic cathodes in AAIBs.

In 2024, Su et al. designed a fully conjugated heterocyclic molecule, tribenzoquinoxaline-5,10-dione (3BQ), derived from 9,10-anthraquinone (AQ), featuring both carbonyl and imine groups for AAIBs (Figure 16a).[118] The multiple redox centers and expanded π-conjugated framework endowed 3BQ with a high theoretical capacity of 515 mAh g^{-1}. When composited with conductive carbon nanotubes (CNTs) featuring highly delocalized π-bonds, the resulting 3BQ-CNT hybrid exhibited enhanced π-π interactions, improved electronic delocalization, and stabilized molecular packing, facilitating efficient Al^{3+} transport. Consequently, 3BQ-CNTs delivered 445.84 mAh g^{-1} at 0.05 A g^{-1} and maintained 125.7 mAh g^{-1} after over 4000 cycles at 1.0 A g^{-1}, with a per-cycle decay rate of 0.011% (Figure 16b-c).

Building on this hybrid design concept, Lu et al. synthesized DDQP, a π-conjugated planar carbonyl and imine conjugated backbone, via dehydration condensation of phenanthrenequinone (PQ) and 2,3,5,6-tetraaminocyclohexa-2,5-diene-1,4-dione (TABQ) (Figure 16d).[119] Theoretical calculations revealed that DDQP exhibits higher electronic density of states near the Fermi level, a lower lowest unoccupied molecular orbital (LUMO) energy, and a reduced LUMO-HOMO gap than its precursors, indicating stronger electron affinity and improved charge transport ability (Figure 16e). Electrochemical measurements revealed that DDQP delivered 239.54 mAh g^{-1} at 400 mA g^{-1}, nearly twice that of PQ and TABQ (Figure 16f), along with improved rate capability and cycling stability. Similarly, Hu et al. synthesized BQPT (benzo[i]benzo[6,7]quinoxalino[2,3,9,10]phenanthrol[4,5-abc]phenazine-5,10,16,21-tetraone), a multi-redox hybrid containing four carbonyl and four imine groups, via a dehydration condensation strategy.[120] Both C=O and C=N groups participate in redox processes during discharge, collectively accepting eight electrons and coordinating with eight $Al(OTF)_2^+$ cations (Figure 16g). This multi-electron mechanism enabled a high capacity of 321.71 mAh g^{-1} at 0.4 A g^{-1} (Figure 16h). Therefore, rational functional group integration and conjugated backbone design offer a feasible and effective route to enhance the electrochemical performance of organic cathodes.

Overall, these studies demonstrate that incorporating both carbonyl and imine groups within an extended π-conjugated framework is an effective strategy to enhance the electrochemical performance of AAIBs cathodes. Such hybrid molecular design overcomes the limitations of single-type redox centers, providing a promising pathway for the development of high-performance organic cathodes for AAIBs. Nevertheless, both small and macro-molecular organic cathodes are prone to dissolution, which can be mitigated by incorporating them into conductive polymers, as discussed in the following section.

3.4.4 Conductive polymers

Conductive polymers, including polyaniline (PANI), polypyrrole (PPy), and polythiophene (PTh), have attracted increasing attention in aqueous batteries owing to their unique π-conjugated backbones and favorable electrochemical reversibility.[121, 122] Compared with small-molecule organic cathodes, conductive polymers possess higher molecular weights and stronger intermolecular interactions, which help mitigate dissolution. Their continuous conjugated skeleton

View Article Online
DOI: 10.1039/D5SC09176D

facilitates electronic transport along the polymer chains and supports rapid and reversible electrochemical reactions. Furthermore, the molecular structures of conductive polymers can be flexibly tuned via monomer design and copolymerization, enabling improvements in specific capacity, conductivity, and cycling stability.

Building on this foundation, in 2022, Sariyer et al. synthesized poly(o-phenylenediamine) (PoPD) via electropolymerization. Using 0.25 M $AlCl_3$ as the electrolyte in a three-electrode system, PoPD delivered an average discharge potential of -0.20 V and a capacity of 156 mAh g^{-1} at 5C (Figure 17a).[123] Even after 1000 cycles, 110 mAh g^{-1} was retained (Figure 17b), demonstrating excellent cycling stability. Building upon this, Meng et al. functionalized PANI with sulfonic acid groups to obtain SPANI, which enhanced both conductivity and ion-polymer interactions.[124] In an aqueous deep eutectic electrolyte composed of $Al(ClO_4)_3 \cdot 9H_2O$ and succinonitrile (SN), SPANI exhibited a capacity of 185 mAh g^{-1} at 0.1 A g^{-1}, outperforming pristine PANI (143 mAh g^{-1}) (Figure 17c), and retained 165 mAh g^{-1} with 89% capacity retention after 300 cycles. XPS analysis revealed that the redox mechanism: during charging, the reduced -NH- groups in SPANI were oxidized to -NH^+- and =NH^+-, which coordinated with ClO_4-, while during discharging, the oxidized groups were reduced back and coordinated with Al^{3+} (Figure 17d). This study highlighted incorporating -SO_3H group simultaneously improved conductivity, ion interaction and electrochemical reversibility, offering valuable guidelines for the molecular design of conductive polymers cathodes.

Extending these advances, Wang et al. developed carbon-supported poly(2,3-diaminophenazine) (PDAP) cathodes via electropolymerization (Figure 17e).[125] The PDAP framework, containing C=N and -NH- groups, provided abundant redox-active sites. In 1 M $Al(ClO_4)_3$ electrolyte, the Al//PDAP cell delivered a high capacity of 338 mAh g^{-1} at 0.2 A g^{-1}, and maintained 233 mAh g^{-1} after 100 cycles. Even at 2 A g^{-1}, 86 mAh g^{-1} was retained after 1000 cycles (65% retention). PDAP also exhibited excellent temperature tolerance, delivering 155 mAh g^{-1} at -20 °C and up to 348 mAh g^{-1} at 45 °C. These outstanding properties originated from the strong π-π stacking and N-H···N hydrogen bonding among PDAP chains, which suppressed dissolution, as evidenced by UV-vis spectroscopy of electrolyte after soaking (Figure 17g). Theoretical calculations further confirmed that increasing chain length from monomer to tetramer narrowed the bandgap (from 1.525 to 1.058 eV) and increased the density of states near the Fermi level, indicating enhanced electron delocalization and faster charge transfer (Figure 17h). This work not only provided a promising strategy for designing high-performance organic cathodes for AAIBs, but also demonstrated their stable operation over a wide temperature range.

Overall, these studies illustrate the versatility of conductive polymers as AAIBs cathodes. Progressing from PoPD to functionalized PANI and PDAP, rational molecular design through functional group incorporation and extension of the conjugated backbone has proven effective in improving capacity, conductivity, and cycling stability. These findings highlight conductive polymers as a tunable platform for designing robust, high-performance organic cathodes for AAIBs.

3.4.5 Radical polymers

Radical polymers represent a class of organic cathode materials, typically composed of aliphatic polymer backbones with redox-active side groups. Unlike conventional conductive polymers, their electrochemical activity primarily arises from reversible redox reactions between the free radicals or oxoammonium ions on the side chains, allowing for stable potential output during charge-discharge processes.[126, 127] The most representative system is based on 2,2,6,6-

View Article Online
DOI: 10.1039/D5SC09176D

tetramethylpiperidin-1-oxyl (TEMPO) side groups, which exhibit high redox potentials and fast electron-transfer kinetics.[128] However, TEMPO is prone to disproportionation under acidic conditions, limiting their applicability in acidic AAIBs electrolytes.

In 2023, Jiang et al. systematically investigated the electrochemical behavior of TEMPO radicals in both organic and aqueous media.[129] They found that TEMPO undergoes irreversible disproportionation in acetonitrile due to the formation of aminoxyl anions ($TEMPO^-$), which coordinate with excess $Al(OTf)_3$, rendering the redox process irreversible. In contrast, in aqueous electrolytes, $TEMPO^-$ in $[Al(OTf)_3 \cdot TEMPO]^-$ can be substituted by OH^- or water molecules, enabling a fully reversible $TEMPO^+/TEMPO^-$ redox cycle and preserving the radical activity (Figure 17f). Building on this understanding, the authors prepared the first TEMPO radical polymer cathode, poly(TEMPO methacrylate) (PTMA). In 1 M $Al(OTf)_3$ electrolyte, PTMA cathode delivered a discharge capacity of approximately 120 mAh g^{-1} at 4C, and retained 77 % after 800 cycles, corresponding to a low per-cycle decay rate of 0.028% (Figure 17i-j). This work highlights the critical role of aqueous environments in stabilizing TEMPO radicals and demonstrates the potential of non-conjugated radical polymers as high-performance cathodes for AAIBs. Overall, the electrochemical performance of various cathode materials discussed in this review is summarized in Table 1.

4. Summary and prospects

AAIBs as an emerging electrical energy storage technology, combine high safety, environmental friendliness and low cost, demonstrating promising potential for green energy applications. Despite notable progress in electrode material design and electrolyte optimization in recent years, the development of AAIBs remains at an early stage, and their commercial deployment is still a considerable distance away. Key limiting factors include the sluggish migration kinetics of multivalent Al^{3+}, as well as insufficient structural reversibility of cathode materials during repeated charge/discharge cycles, which lead to capacity fading and restricted cycle life. These issues significantly constrain AAIBs from achieving high capacity, high power density, and long-term stability.

Regarding cathode materials, different types exhibit distinct structural features and ion/electron transport properties, which determine their electrochemical performance and associated challenges. This review systematically summarizes recent advances in AAIBs cathode materials, focusing on four representative systems: manganese-based oxides, vanadium-based compounds, PBAs, and organic materials. Specifically:

(1) Manganese oxides are among the most widely studied AAIBs cathodes due to their abundance, low cost, diverse crystal structures and multiple electron-transfer capability. Layered δ-MnO_2, with large interlayer spacing and two-dimensional diffusion channels, facilitates Al^{3+} diffusion and generally exhibits high specific capacity, whereas tunnel-type MnO_2 (α, β, γ) with narrower channels limits Al^{3+} diffusion and storage, resulting in lower capacity and sluggish kinetics. Although layered structures offer higher capacity, they often suffer structural instability during cycling, undergoing in situ phase transformations to thermodynamically more stable Al_xMnO_2 phases. While this process can partially relieve lattice strain, it often causes capacity decay. Unmodified MnO_2 cathodes can deliver initial capacities of 500-600 mAh g^{-1}, but structural collapse and Mn dissolution hinder stable cycling beyond 200 cycles. Strategies such as molecular or metal-

View Article Online
DOI: 10.1039/D5SC09176D

ion pre-intercalation or doping have been developed to expand interlayer spacing, mitigate lattice strain, enhance structural flexibility, and prolong cycling stability. However, while pre-intercalation or doping strategies can effectively enlarge the interlayer spacing, they may slightly perturb the crystal structure, which could influence long-term structural stability during repeated cycling. In addition, the strong interaction between Al^{3+} ions and the metal-oxygen framework may further affect such structural changes. Future strategies should aim to balance high initial capacity with durable structural integrity.

(2) Vanadium-based cathodes mainly include layered V_2O_5, tunnel-type VO_2, vanadates, and vanadium phosphates. Layered V_2O_5 provides large interlayer spacing conducive to Al^{3+} strorage but suffers from lattice contraction and structural degradation upon cycling. Tunnel-type VO_2 maintains structural integrity but limits ion diffusion due to fixed tunnel size. Vanadates utilize pre-inserted cations as "pillars" to expand interlayer spacing, enhancing structural stability, whereas vanadium phosphates feature robust 3D frameworks but limited electronic conductivity due to $[PO_4]$ units. Overall, V-based materials often exhibit lower capacity than Mn-based oxides. Similar to Mn-based oxides, although strategies such as defect engineering, metal-ion doping, nanoscale structuring, and conductive composite design can improve the electrochemical performance of V-based cathodes, achieving high capacity, fast kinetics, and long-term stability simultaneously remains challenging.

(3) PBAs offer tunable frameworks, long cycle life, and multiple redox-active centers, showing great promise in AAIBs. Depending on the number of active centers, PBAs are classified as single or dual redox-active centers systems. Single-center PBAs are limited by Fe^{2+}/Fe^{3+} charge transfer, with capacities typically in the tens of mAh g^{-1}, while dual-center PBAs leverage multi-metal synergy to achieve capacities above 100 mAh g^{-1}. Their remarkable advantage lies in cycling stability, with thousands to tens of thousands of cycles achievable, far exceeding Mn- and V-based cathodes. Current strategies to enhance performance include defect engineering to improve ion diffusion, entropy regulation to increase structural robustness via multi-metal centers, and nanostructure design to shorten ion transport paths and buffer volume changes. Nevertheless, the relatively low intrinsic capacity of PBAs, together with the limited utilization of redox-active sites, remains a key bottleneck for their application in high-energy AAIBs. Future work should focus on further optimizing framework design to achieve high capacity, high rate, and long lifespan concurrently.

(4) Organic cathodes, composed mainly of C, H, O, and N, possess tunable molecular backbones and flexible structures, alleviating volume strain during charge/discharge. Compared with the strong electrostatic interactions in inorganic cathodes, weak coordination or ion-dipole interactions within the organic framework facilitating Al^{3+} ion migration. Energy storage relies on reversible redox-active functional groups, such as carbonyls, imines, or TEMPO radicals. Based on the type of redox-active site, organic cathodes are categorized into quinone-based compounds, N-heteroaromatics, π-conjugated carbonyl-imine hybrids, conductive polymers, and radical polymers. Overall, organic materials typically exhibit better cycling stability than inorganic counterparts, with capacities higher than PBAs but lower than Mn oxides. Performance can be improved via functional group integration, backbone conjugation optimization, and conductive composite formation. Nevertheless, challenges such as active material dissolution, limited energy density, and balancing molecular stability with high redox activity still hinder practical applications, calling for rational molecular and composite design to achieve high capacity, fast kinetics, and long-term cycling

View Article Online
DOI: 10.1039/D5SC09176D

stability.

To further advance the development of high-performance AAIBs, future research should focus on the following directions:

(1) **Design and optimization of cathode materials.** The structural and chemical characteristics of the cathode critically govern Al^{3+} accessibility, migration kinetics, and the reversibility of Al^{3+}-cathode interactions. For inorganic cathodes, strategies such as defect engineering, molecular pre-intercalation, heteroatom doping, and conductive network construction should be further explored to expand interlayer spacing, stabilize frameworks, and create flexible coordination environments. Importantly, future efforts should emphasize establishing clear structure-chemistry-electrochemistry relationships, enabling predictive and rational cathode design. These approaches are expected to mitigate lattice strain during Al^{3+}-cathode interactions and enhance charge transfer, enabling higher capacity, improved rate capability, and long-term cycling stability. For organic cathodes, future research should focus on the rational design of multifunctional groups and the modulation of molecular backbone flexibility to facilitate more Al^{3+} interactions with active sites. Combined with optimized π-conjugation and conductive composite formation, these strategies can improve ion/electron transport, suppress dissolution, and achieve synergistic enhancements in electrochemical performance. Overall, a multiscale, material-tailored design strategy offers a promising pathway toward high-performance and durable AAIBs cathodes.

(2) **Mechanism insight through advanced characterization and theoretical modeling.** In situ techniques (XRD, XAS, Raman, etc.) combined with first-principles calculations and molecular dynamics simulations can provide atomic-level understanding of ion migration pathways, redox mechanisms, and interfacial processes. Particular attention should be placed on distinguishing Al^{3+}-dominated storage from proton-assisted or co-insertion mechanisms, which remains a key challenge in aqueous systems. Correlating structural evolution induced by Al^{3+}-cathode interactions with electrochemical performance will offer theoretical guidance for rational cathode design.

(3) **Sustainable materials and scalable device engineering.** Research should integrate material sustainability with device-level optimization, bridging laboratory studies and practical applications. Development of earth-abundant, environmentally friendly, and low-cost materials, including bio-derived organic and inorganic-organic hybrid frameworks, will enhance AAIBs sustainability. Simultaneously, full-cell design optimization and systematic evaluation of long-term stability, safety, and durability under realistic conditions, including extreme cold or high-temperature environments, are essential. Coordinated design of sustainable materials and scalable devices will provide a solid foundation for the practical deployment of AAIBs in green energy storage.

Author contributions

J. Feng collected papers related to the topic and wrote the manuscript. C. Yu and X. Huang conceived the overall idea of the perspective. The manuscript was revised by all the authors.

Conflict of interest

There are no conflicts to declare.

Acknowledgments

The authors acknowledge the support from the Australian Research Council, Queensland node of

View Article Online
DOI: 10.1039/D5SC09176D

the NCRIS-enabled Australian National Fabrication Facility (ANFF), the Centre for Microscopy and Microanalysis, The University of Queensland.

View Article Online
DOI: 10.1039/D5SC09176D

Figures

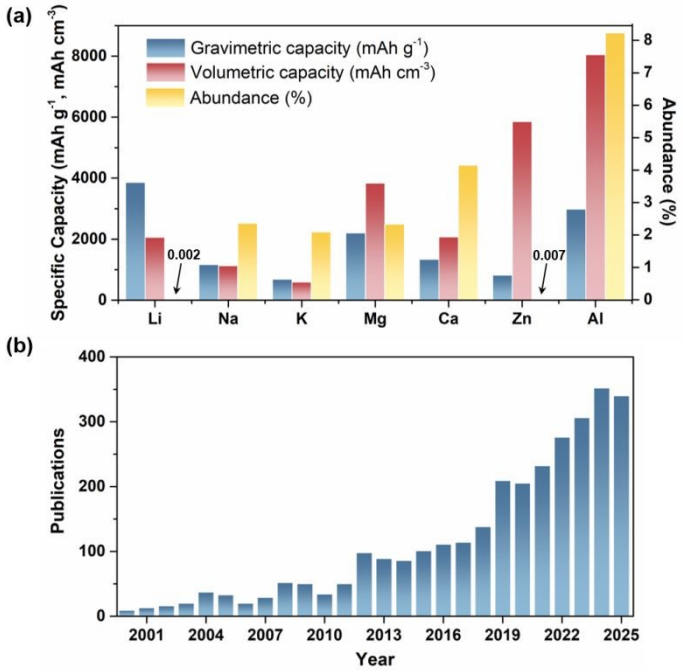

Figure 1 (a) Comparison of different metal anodes in terms of gravimetric capacity, volumetric capacity and earth's crust abundance. (b) Publication trends of aqueous aluminum-ion batteries from 2000 to 2025. Data were obtained from the Web of Science using the search keywords "aqueous aluminum-ion battery", "aqueous aluminum ion battery", or "AAIB".

View Article Online
DOI: 10.1039/D5SC09176D

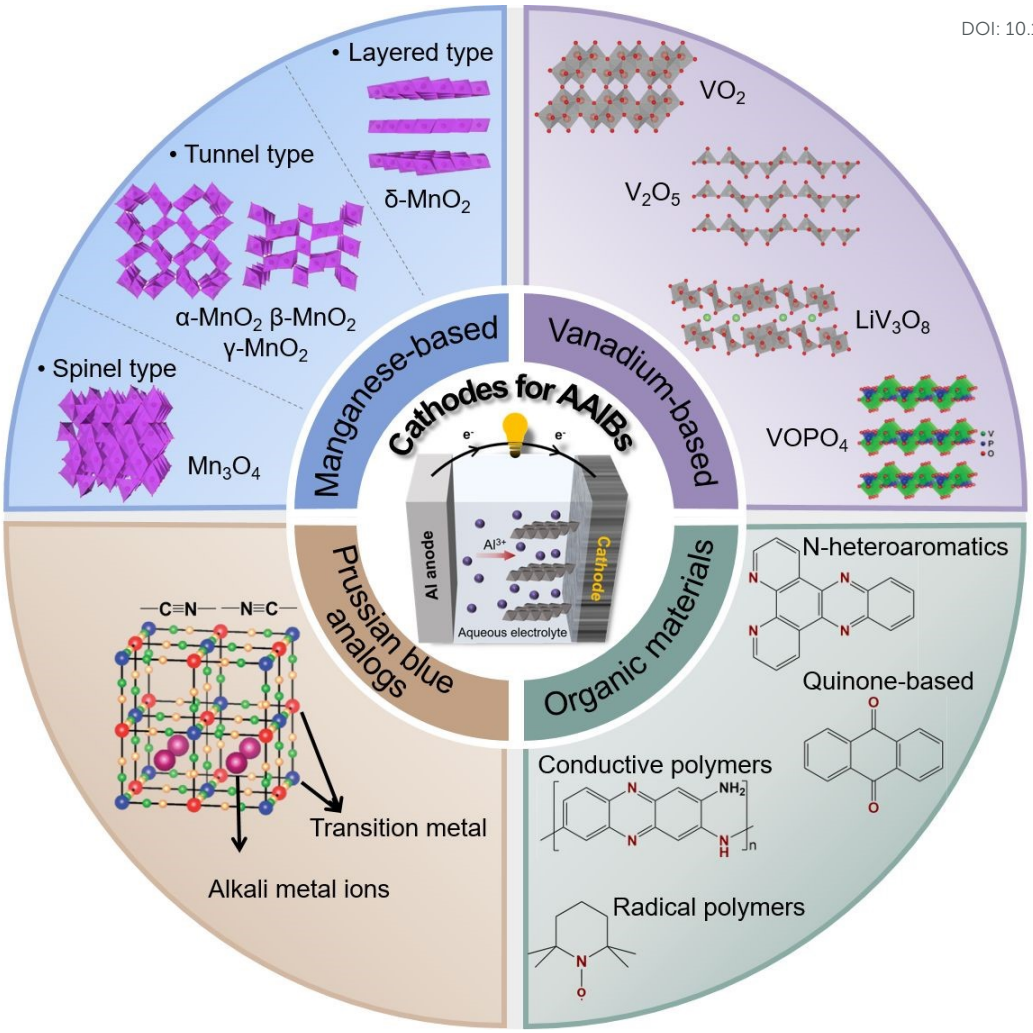

Figure 2 Representative categories of cathode materials developed for AAIBs.

View Article Online
DOI: 10.1039/D5SC09176D

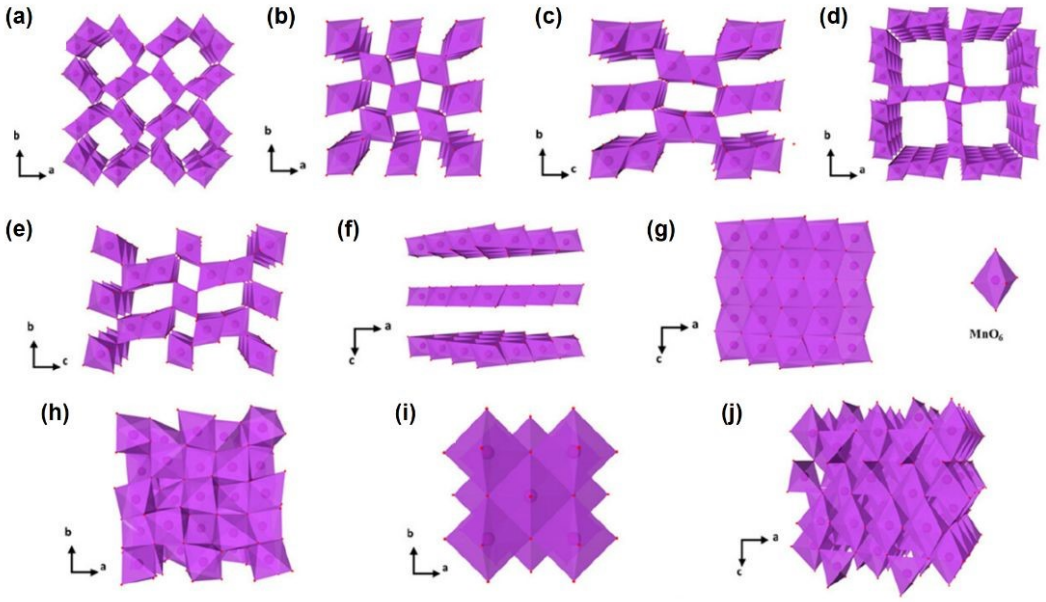

Figure 3 Crystal structures of (a) α-MnO_2, (b) β-MnO_2, (c) R-MnO_2, (d) T-MnO_2, (e) γ-MnO_2, (f) δ-MnO_2, (g) ε-MnO_2, (h) Mn_2O_3, (i) MnO, and (j) Mn_3O_4 are displayed. Reproduced with permission.[41] Copyright 2024, American Chemical Society.

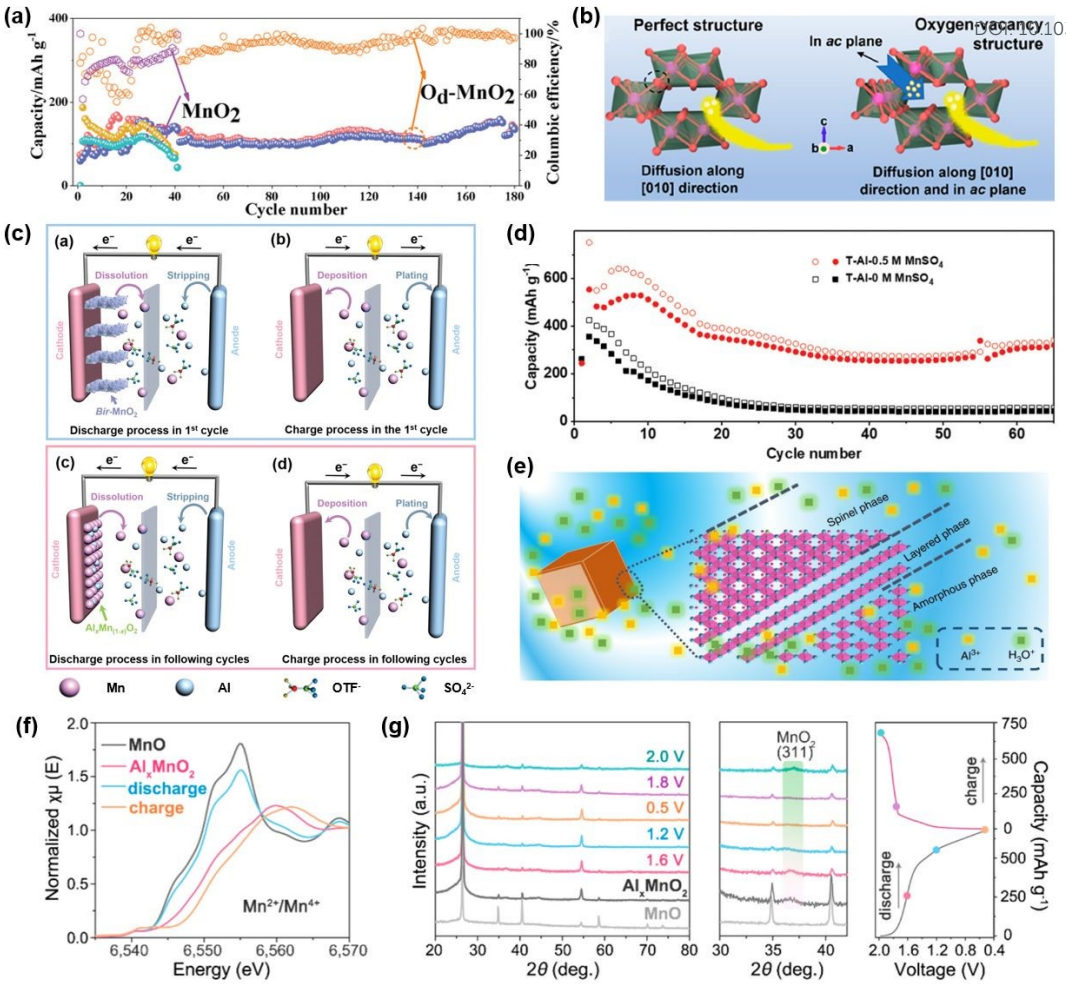

Figure 4 (a) Cycling performance of O_d-MnO_2 and MnO_2 at 500 mA g^{-1}. Reproduced with permission.[46] Copyright 2024, Wiley-VCH. (b) Diffusion of H^+ into the perfect structure of MnO_2 and the structure of MnO_2 with an oxygen vacancy. Reproduced with permission.[47] Copyright 2023, American Chemical Society. (c) The schematic diagram of aluminum-manganese electrochemistry in the first discharge process, the first charge process, and the discharge process and charge process in following cycles. (d) Cycling performance of the T-Al/δ-MnO_2 and T-Al/0.5Mn/δ-MnO_2 batteries. Reproduced with permission.[48] Copyright 2019, Wiley-VCH. (e) The schematic profile of the structure of $Al_xMnO_2 \cdot nH_2O$. Reproduced with permission.[52] Copyright 2019, Springer Nature. (f) Mn K-edge XANES spectra of Al_xMnO_2 cathodes after full discharge and charge. (g) XRD patterns of Al_xMnO_2 cathodes at selected states during the first cycle and typical charge/discharge curves at 100 mA g^{-1}. Reproduced with permission.[53] Copyright 2020, American Chemical Society.

View Article Online
DOI: 10.1039/D5SC09176D

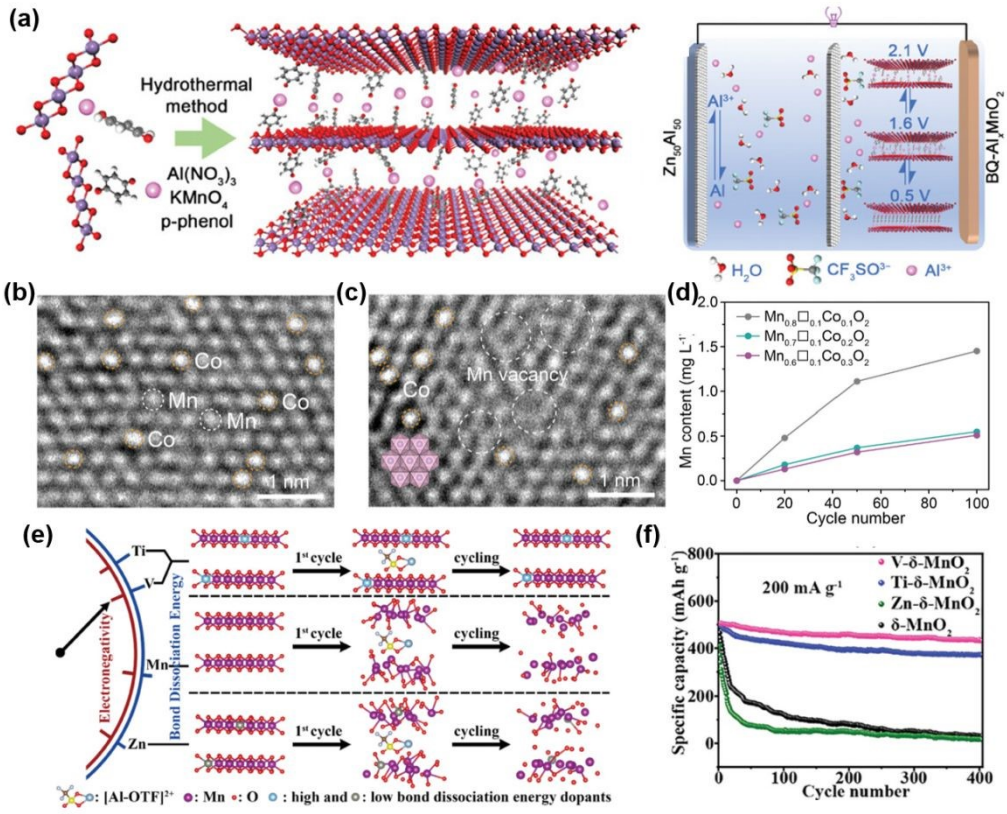

Figure 5 (a) Schematic illustration of preparation of layered BQ-Al_xMnO_2 by a hydrothermal method, during which highly coordinated BQ-Al^{3+} pre-intercalated in MnO_2 layers, and scheme of aqueous AIB full cell that is composed of $Zn_{50}Al_{50}$ alloy anode and titanium foil-supported BQ-Al_xMnO_2 cathode, with 2 M $Al(OTf)_3$ solution as aqueous electrolyte. Reproduced with permission.[55] Copyright 2024, Wiley-VCH. Atomic-resolution HAADF-STEM images of (b) $Mn_{0.8}Co_{0.2}O_2$ and (c) acid-coagulated $Mn_{0.7}\square_{0.1}Co_{0.2}O_2$. Inset: the hexagonal arrangement of Mn atoms in ideal MnO_2 sheets. (d) ICP-AES measurement of dissolved manganese in 2 M $Al(OTF)_3$ electrolyte after different number of cycles. Reproduced with permission.[59] Copyright 2023, Wiley-VCH. (e) Schematic illustration of the impact of heteroatoms doping on the electrochemical stability and performance of δ-MnO_2 cathodes during AAIBs cycling. (f) Electrochemical cycling performances of pristine and doped δ-MnO_2 cathodes at 200 mA g^{-1}. Reproduced with permission.[60] Copyright 2024, Wiley-VCH.

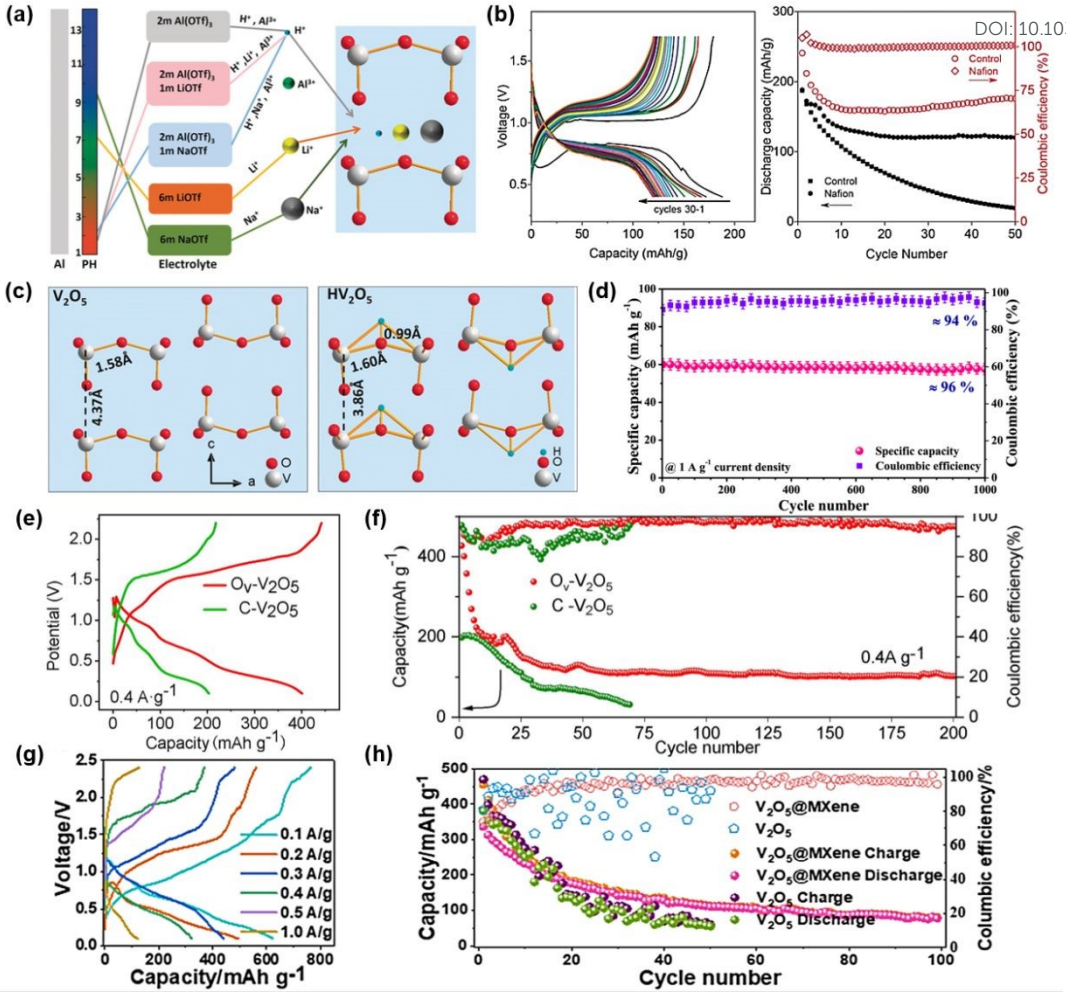

Figure 6 (a) Different cation intercalating behaviors of V_2O_5 through regulating the electrolytes. (b) alvanostatic discharge/charge profiles of aqueous Al/V_2O_5 batteries using Nafion modified separator and corresponding cycling performance and coulombic efficiency. (c) Structure of pristine V_2O_5 and after proton insertion. Reproduced with permission.[38] Copyright 2020, Wiley-VCH. (d) Cycling stability performance of the synthesized V_2O_5 material. Reproduced with permission.[64] Copyright 2023, American Chemical Society. (e) The initial GCD curves for O_v-V_2O_5 and C-V_2O_5 at 0.4 A g^{-1} and (f) cycling performance at 0.4 A g^{-1}. Reproduced with permission.[65] Copyright 2025, Elsevier. (g) Rate performance of V_2O_5@Mxene and (h) Comparison of the cycle performance between V_2O_5@MXene and V_2O_5 at 0.4 A g^{-1}. Reproduced with permission.[66] Copyright 2024, American Chemical Society.

View Article Online
DOI: 10.1039/D5SC09176D

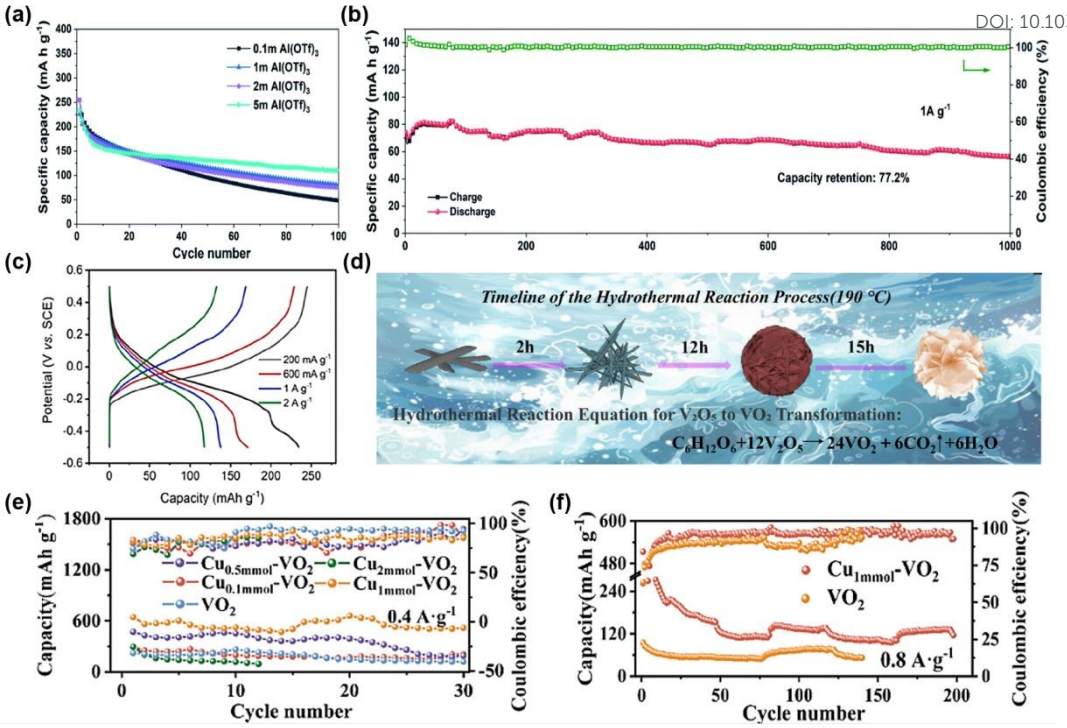

Figure 7 (a) cycling performances of the VO_2-B electrodes in the $Al(OTF)_3$ electrolytes with different concentrations at 150 mA g^{-1}. (b) long-term cycling performance of the VO_2-B electrodes at 1 A g^{-1} in the 5 M $Al(OTF)_3$ electrolyte. Reproduced with permission.[69] Copyright 2020, Royal Society of Chemistry. (c) GCD curve of VO_2 at different current densities. Reproduced with permission.[70] Copyright 2021, Elsevier. (d) Schematic diagram of preparation and morphology evolution of Cu_{1mmol}-VO_2. (e) Cycling performance at 0.4 A g^{-1}. (f) Cycling performance of VO_2 and Cu_{1mmol}-VO_2 at 0.8 A g^{-1}. Reproduced with permission.[71] Copyright 2025, Wiley-VCH.

View Article Online
DOI: 10.1039/D5SC09176D

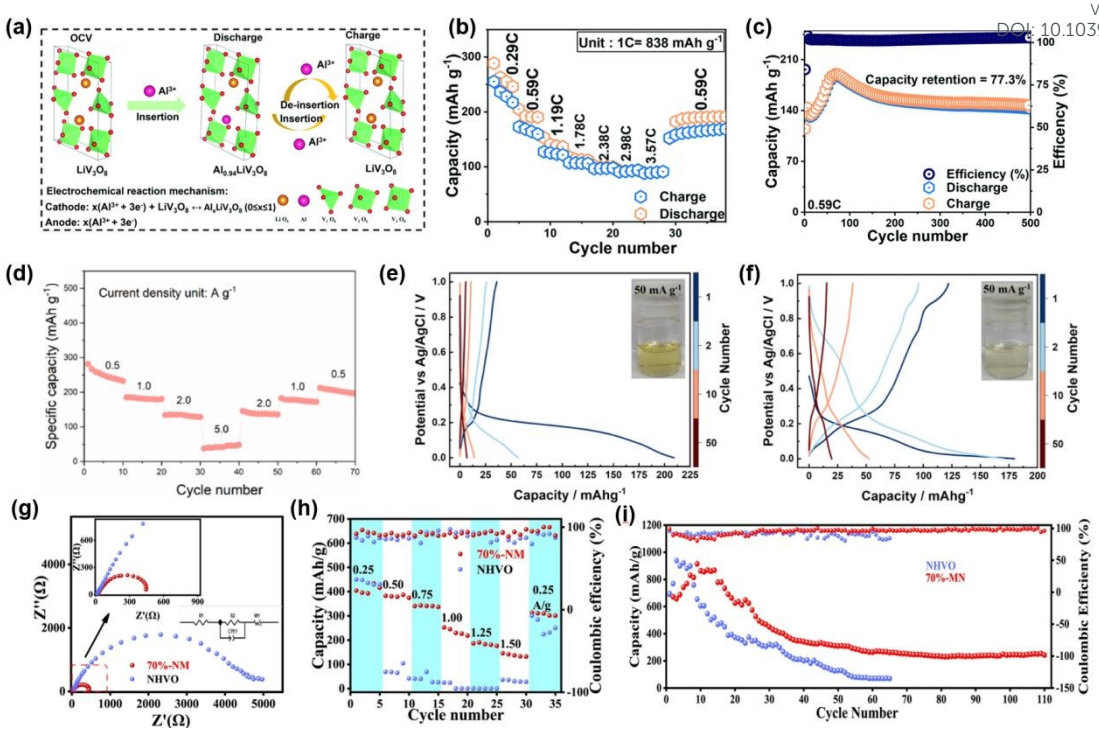

Figure 8 (a) Schematic representation of the Al^{3+} storage properties of the LiV_3O_8 cathode during the charge and discharge course. (b) rate performances of the LiV_3O_8 at different current densities and (c) cycle life curve at 0.59 C. Reproduced with permission.[72] Copyright 2022, Royal Society of Chemistry. (d) Rate tests of layered $NH_4V_4O_{10}$ nanosheets at sets of current densities from 0.5 to 5 A g^{-1}. Reproduced with permission.[73] Copyright 2023, Elsevier. (e-f) GCD (current density = 50 mA g^{-1}) profile of $NH_4V_4O_{10}$ electrodes cycled in 1 M $AlCl_3$ (e) and 1 M $AlCl_3$ + 0.5 M NH_4Cl (f) electrolytes, respectively. Reproduced with permission.[74] Copyright 2024, American Chemical Society. (g) Multiplicity curve of 70 %-NM ($(NH_4)_2V_{10}O_{25}\cdot 8H_2O/Ti_3C_2T_x$ composites). (h) Rate performance of 70 %-NM and NHVO ($(NH_4)_2V_{10}O_{25}\cdot 8H_2O$). (i) Cyclic performance graphs for 70 %-NM and NHVO. Reproduced with permission.[75] Copyright 2024, Elsevier.

View Article Online
DOI: 10.1039/D5SC09176D

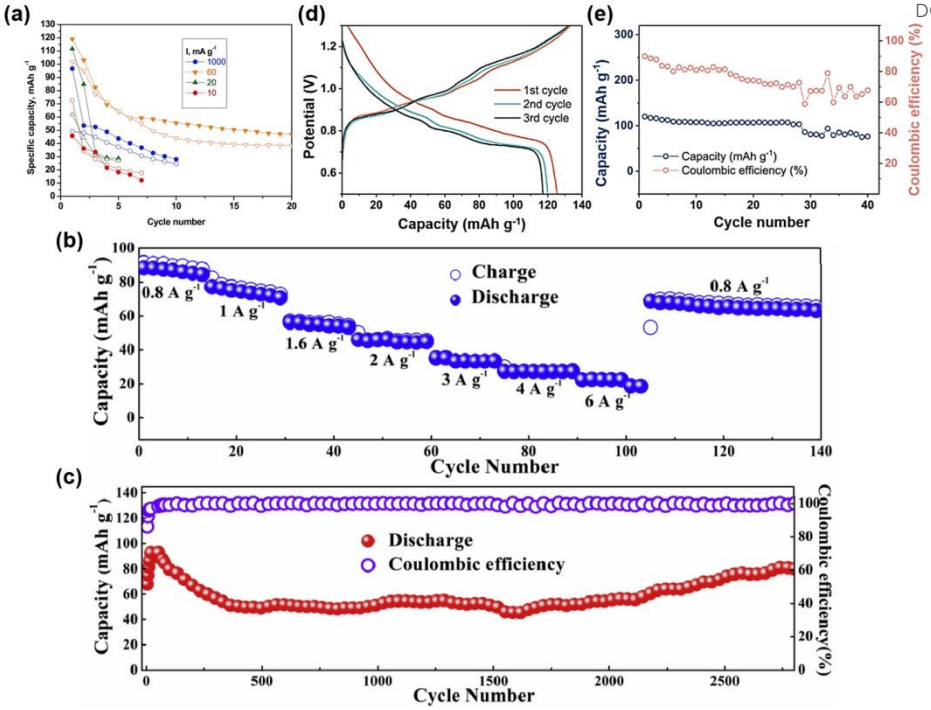

Figure 9 (a) Capacity-cycle number at several rates of $Na_3V_2(PO_4)_3$ (charge: open symbols, discharge: closed symbols). Reproduced with permission.[78] Copyright 2018, Elsevier. (b) Rate capability at various rates and (c) long-term cycling performance and the corresponding coulombic efficiency at 1 A g^{-1} of the rechargeable solid-state aqueous AIB. Reproduced with permission.[79] Copyright 2020, Elsevier. (d) First three charge/discharge curves and (e) cycling performance of the $VOPO_4 \cdot 2H_2O$/Al metal batteries at a current density of 20 mA g^{-1}. Reproduced with permission.[80] Copyright 2021, Elsevier.

View Article Online
DOI: 10.1039/D5SC09176D

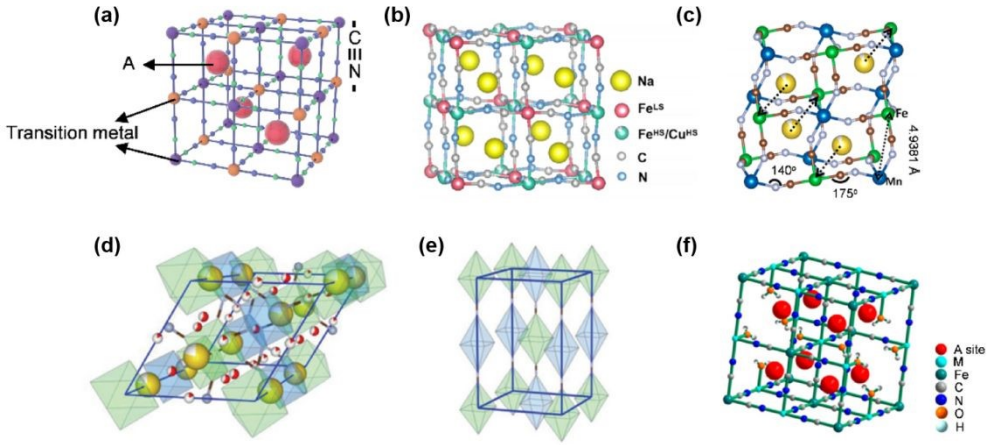

Figure 10 Schematic crystal structures of PBAs: (a) cubic phase, (b) monoclinic phase, (c) rhombohedral phase, (d) trigonal phase, (e) tetragonal phase, and (f) PBA framework with $[Fe(CN)_6]$ vacancies. Reproduced with permission.[86] Copyright 2025, Springer Nature.

View Article Online
DOI: 10.1039/D5SC09176D

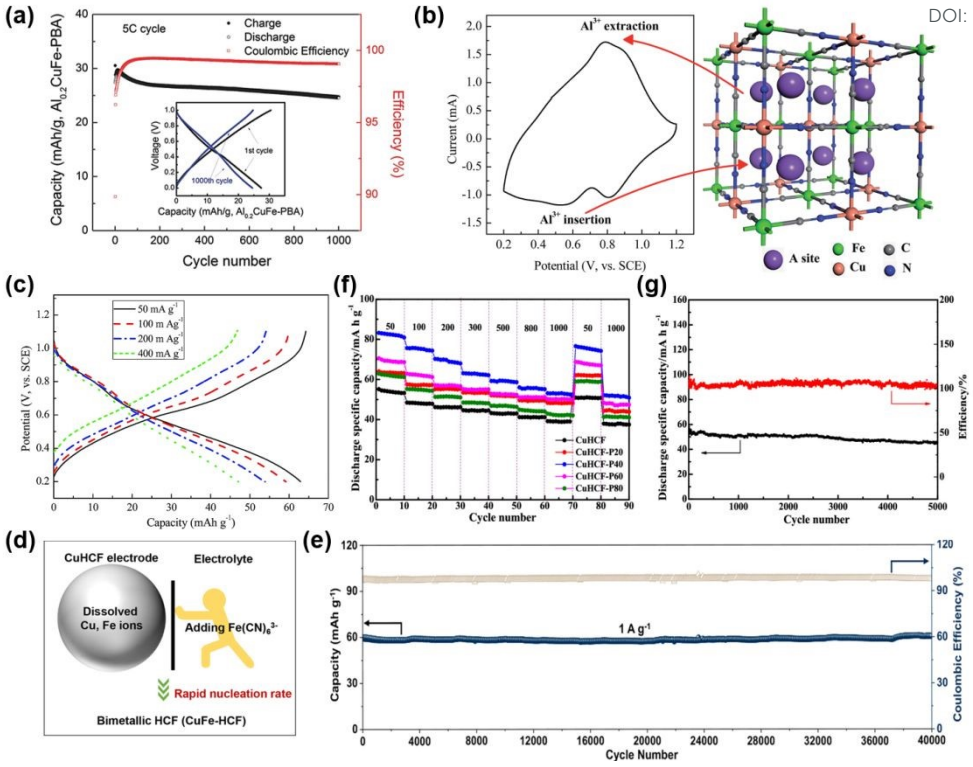

Figure 11 (a) Cycling performance and coulombic efficiency of an AC/$Al_{0.2}$CuFe-PBA cell at a 5 C rate. The inset figure shows the 1st and 1000th charge and discharge curves. Reproduced with permission.[89] Copyright 2015, Wiley-VCH. (b) Typical CV curve of the CuHCF electrode in aqueous $Al_2(SO_4)_3$ and the schematic positions of Al^{3+} in CuHCF framework and (c) Charge/discharge curves at different current densities of the CuHCF electrode in 0.5 M $Al_2(SO_4)_3$ aqueous solution. Reproduced with permission.[90] Copyright 2015, Royal Society of Chemistry. (d) Schematic diagram of inhibiting metal ions dissolution and (e) long-term stability performance. Reproduced with permission.[91] Copyright 2023, American Chemical Society. (f) The rate performance of the as-prepared samples at the current density of 50-1000 mA g-1 and (g) Cycle performance of at a current density of 1000 mA g^{-1}. Reproduced with permission.[93] Copyright 2023, American Chemical Society.

View Article Online
DOI: 10.1039/D5SC09176D

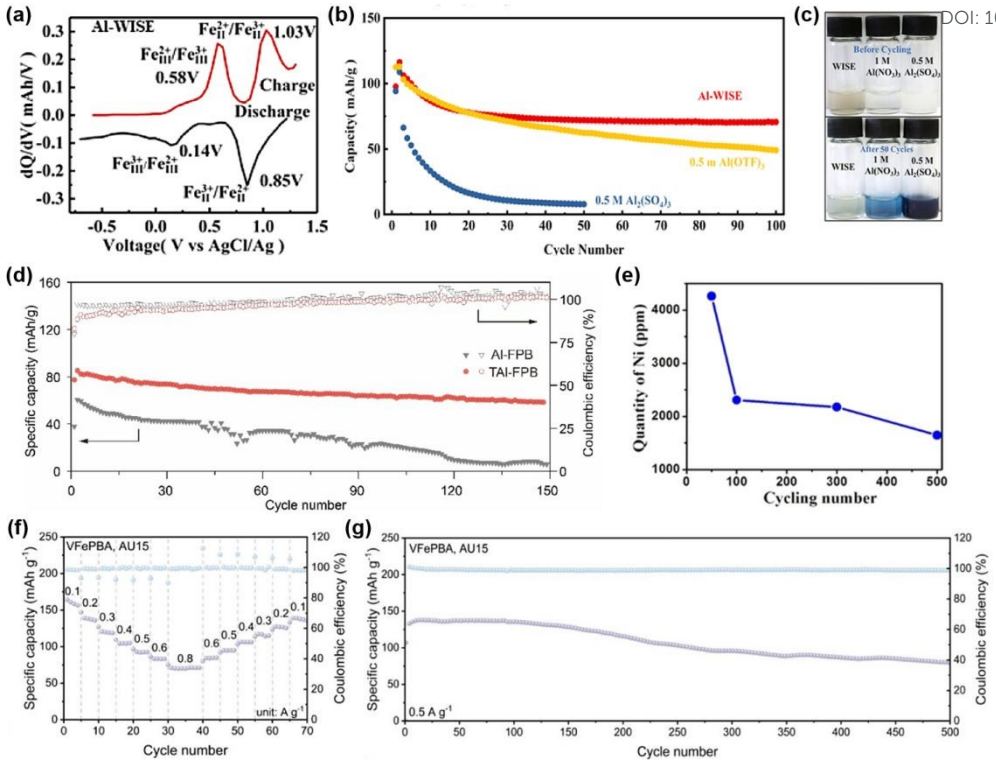

Figure 12 (a) The differential profiles of the 50th cycle in Al-WISE. (b) Cycling life and Coulombic efficiency of the FF-PBA cathode in Al-WISE, 0.5 M $Al_2(SO_4)_3$, and 0.5 M $Al(OTF)_3$ electrolytes. (c) The cathode dissolution experiment. The upper photos are before cycling and the bottom photos are after 50 cycles. Reproduced with permission.[95] Copyright 2019, American Chemical Society. (d) Cycling performance and corresponding coulombic efficiency of aqueous Al-FPB batteries using Al and TAl with 2 M $Al(OTF)_3$ at 100 mA g^{-1}. Reproduced with permission.[96] Copyright 2021, Elsevier. (e) Ni dissolution concentration from the KNHCF electrode after the 50th, 100th, 300th, 500th cycle measured by ICP-OES. Reproduced with permission.[97] Copyright 2020, Wiley-VCH. (f) Capacitive contribution ratios of VFePBA at various scan rates. (g) Long-term cycling performance of VFePBA. Reproduced with permission.[98] Copyright 2025, Wiley-VCH.

View Article Online
DOI: 10.1039/D5SC09176D

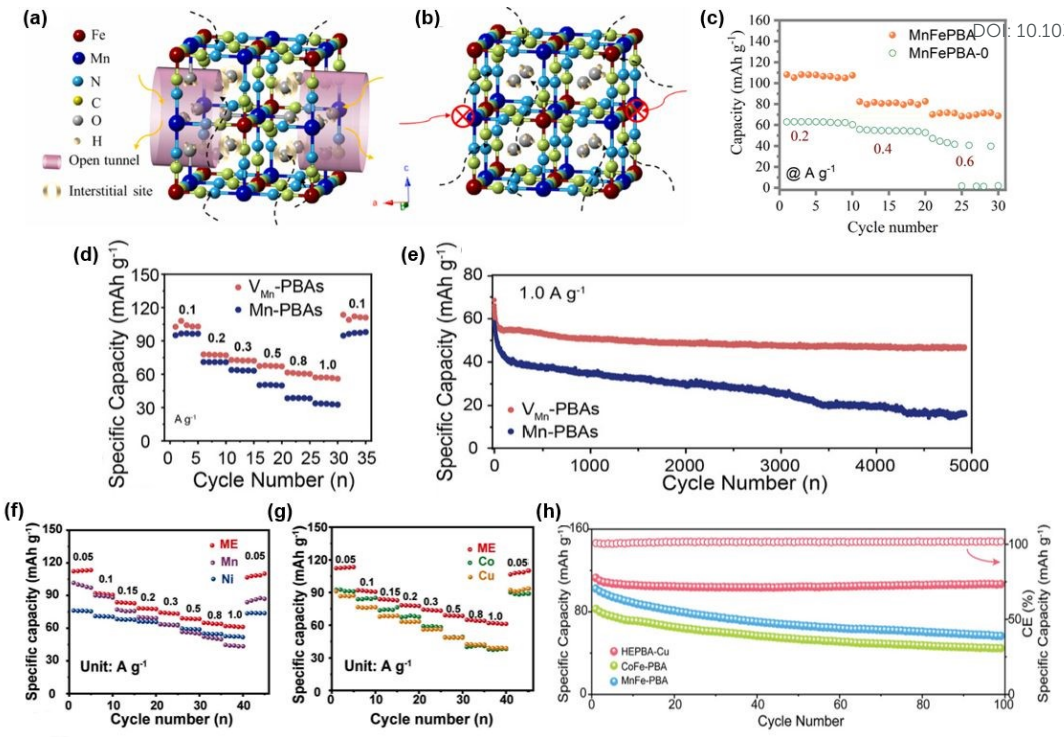

Figure 13 (a) Corresponding crystal structure of MnFe-PBA unit cell. The yellow and pink hollow cylinders are used to mark interstitial sites for intercalated ions and enlarged open tunnels for the diffusion of carriers, respectively. (b) Corresponding crystal structure of a non-defective MnFe-PBA unit cell, and the possible pathways for Al ion ingress. (c) The effects of vacancy on the rate performance. MnFePBA is with vacancy and MnFePBA-0 is a non-defective material. Reproduced with permission.[99] Copyright 2021, Elsevier. (d) Rate performance and (e) Long-term cyclic stability of the PBAs//AC cell at 1 A g^{-1}. Reproduced with permission.[100] Copyright 2025, Wiley-VCH. (f-g) Rate performance at current densities from 0.05 to 1.0 A g^{-1} for ME-PBAs and the different single-metal PBAs. Reproduced with permission.[101] Copyright 2024, Wiley-VCH. (h) Cycling performance of HEPBA-Cu and bimetallic PBA at 1.0 A g^{-1}. Reproduced with permission.[102] Copyright 2024, Wiley-VCH.

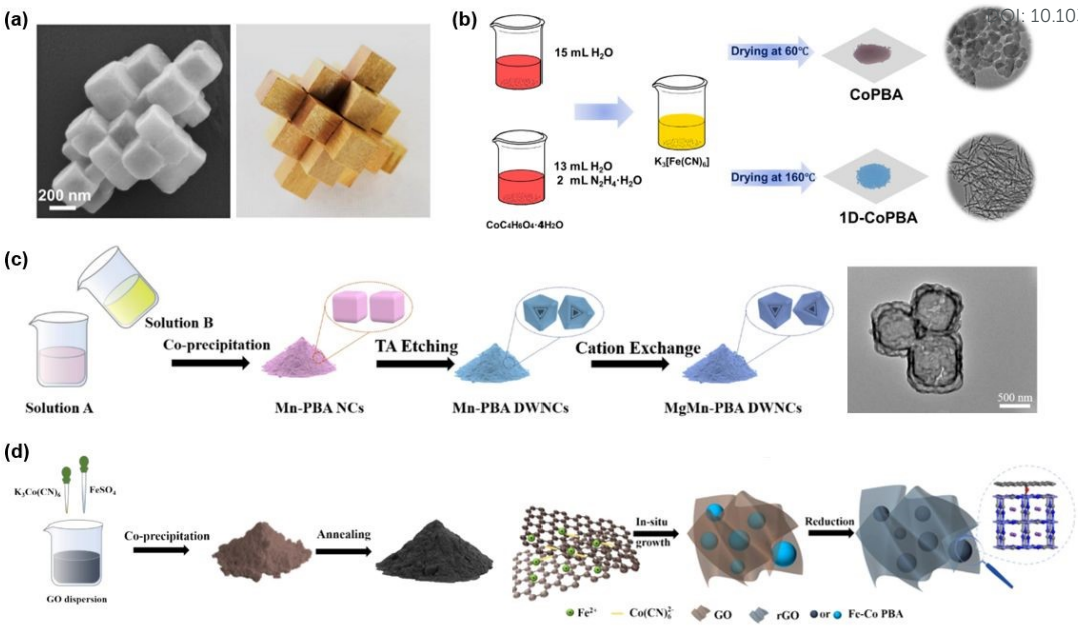

Figure 14 (a) SEM images of the $K_2CoFe(CN)_6$ nanocubic and structure of burr puzzles. Reproduced with permission.[103] Copyright 2020, Elsevier. (b) Schematic Illustration of the Synthesis and Structural Characteristics of the CoPBA and 1D-CoPBA Materials. Reproduced with permission.[104] Copyright 2024, American Chemical Society. (c) Schematic representation of the synthetic process of Mn-PBA NCs, Mn-PBA DWNCs and MgMn-PBA DWNCs, respectively. Reproduced with permission.[105] Copyright 2024, Elsevier. (d) Schematic representation of the synthetic process of Fe-Co PBA/rGO. Reproduced with permission.[106] Copyright 2024, Elsevier.

View Article Online
DOI: 10.1039/D5SC09176D

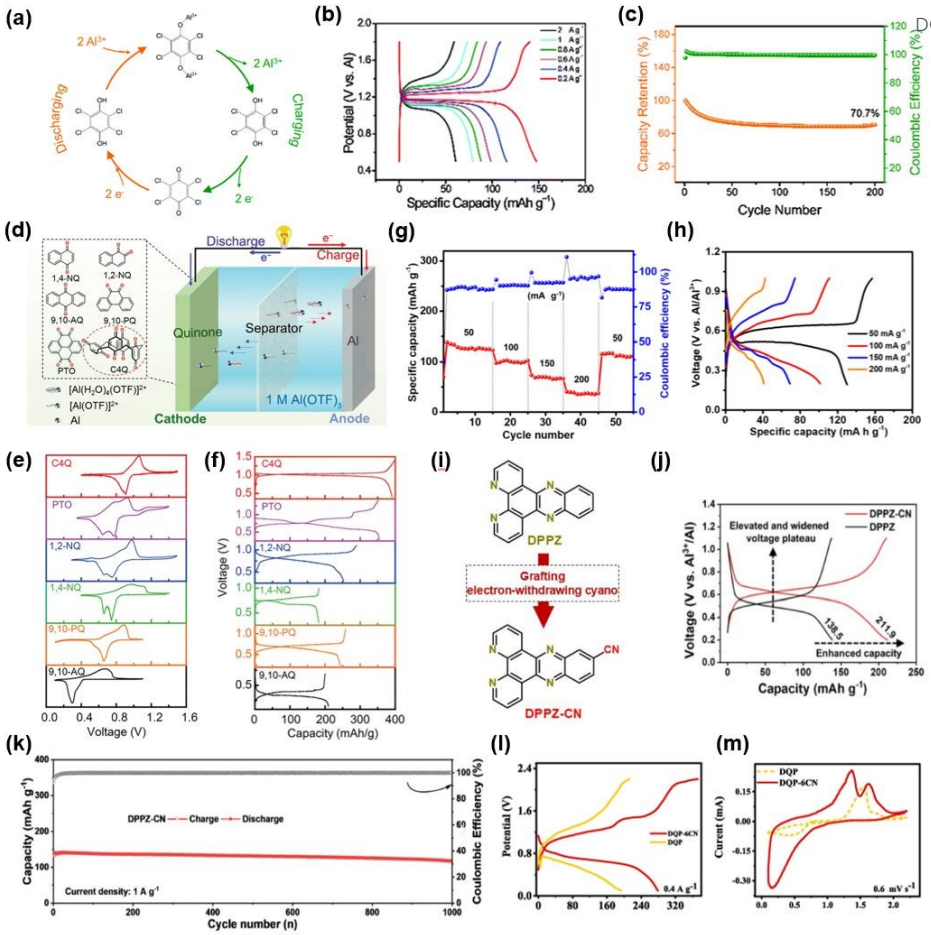

Figure 15 (a) Schematic diagram of the structure transformation of TCQ in the electrochemical process. (b) GCD curves at various current densities and (c) cycling performance of the Al//TCQ battery. Reproduced with permission.[112] Copyright 2021, Royal Society of Chemistry. (d) Schematic illustration of fabricated aqueous Al-quinone batteries. (e) CV curves at 0.1 mV s^{-1} and (f) GCD curves at a current density of 40 mA g^{-1} of different quinone compounds. Reproduced with permission.[113] Copyright 2021, Wiley-VCH. (g) Rate performance of PZ at various current densities from 50 to 200 mA g^{-1} and (h) corresponding discharge/charge curves. Reproduced with permission.[114] Copyright 2021, Wiley-VCH. (i) Typical molecular structure. (j) charge/discharge profiles at 0.1 A g^{-1} for Al//DPPZ-CN and Al//DPPZ batteries with 1 M $Al(ClO_4)_3$ aqueous electrolyte. (k) Long-term cycling performance of Al//DPPZ-CN battery at 1 A g^{-1}. Reproduced with permission.[116] Copyright 2025, Wiley-VCH. (l) GCD curves of DQP-6CN and DQP and (m) CV curves of DQP-6CN. Reproduced with permission.[117] Copyright 2025, Elsevier.

View Article Online
DOI: 10.1039/D5SC09176D

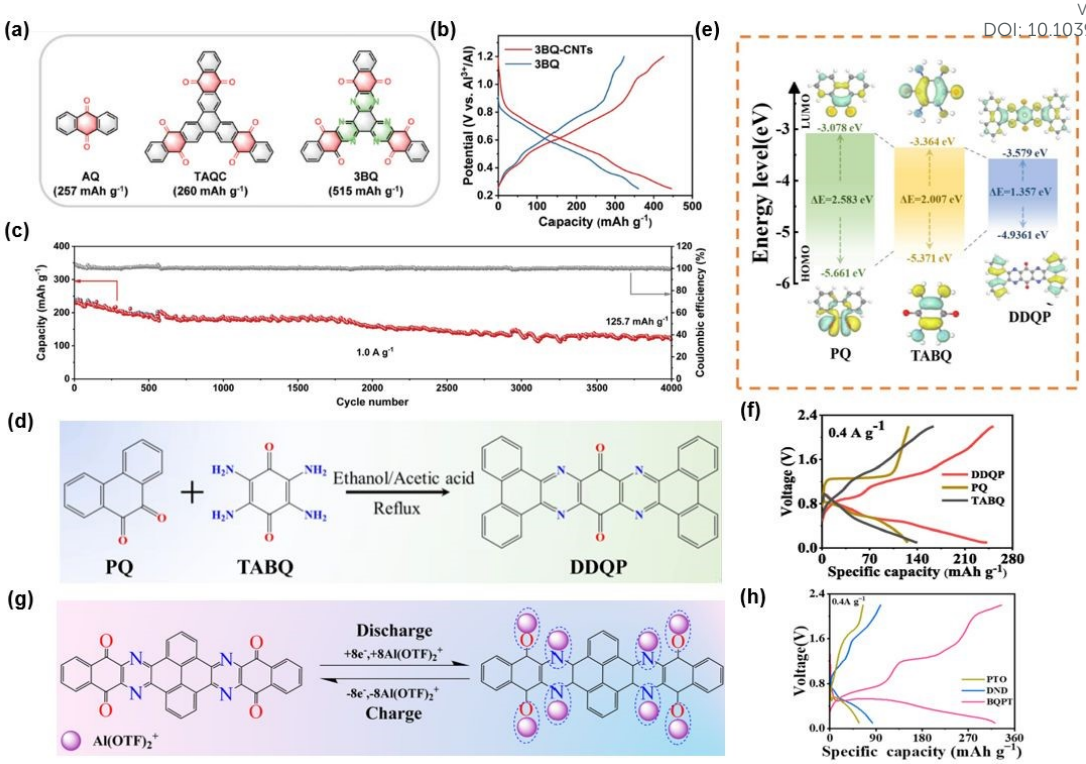

Figure 16 (a) Schematic illustration of molecular design from AQ to TAQC and 3BQ via expanding the π-conjugation strategy. (b) Typical Galvanostatic charge/discharge profiles of the 3BQ-CNTs//Al and 3BQ//Al batteries at 0.05 A g^{-1}. (c) Long-cycle performance of 3BQ-CNTs electrodes at 1.0 A g^{-1}. Reproduced with permission.[118] Copyright 2024, Wiley-VCH. (d) Synthesis pathway of DDQP. (e) LUMO and HOMO of PQ, TABQ and DDQP and energy level gap. (f) First charge/discharge curves of PQ, TABQ and DDQP at 400 mA g^{-1}. Reproduced with permission.[119] Copyright 2024, Elsevier. (g) Mechanistic description of the reversible redox reaction of the BQPT and (h) GCD curves of DND, PTO, and BQPT electrodes at 0.4 A g^{-1}. Reproduced with permission.[120] Copyright 2024, American Chemical Society.

View Article Online
DOI: 10.1039/D5SC09176D

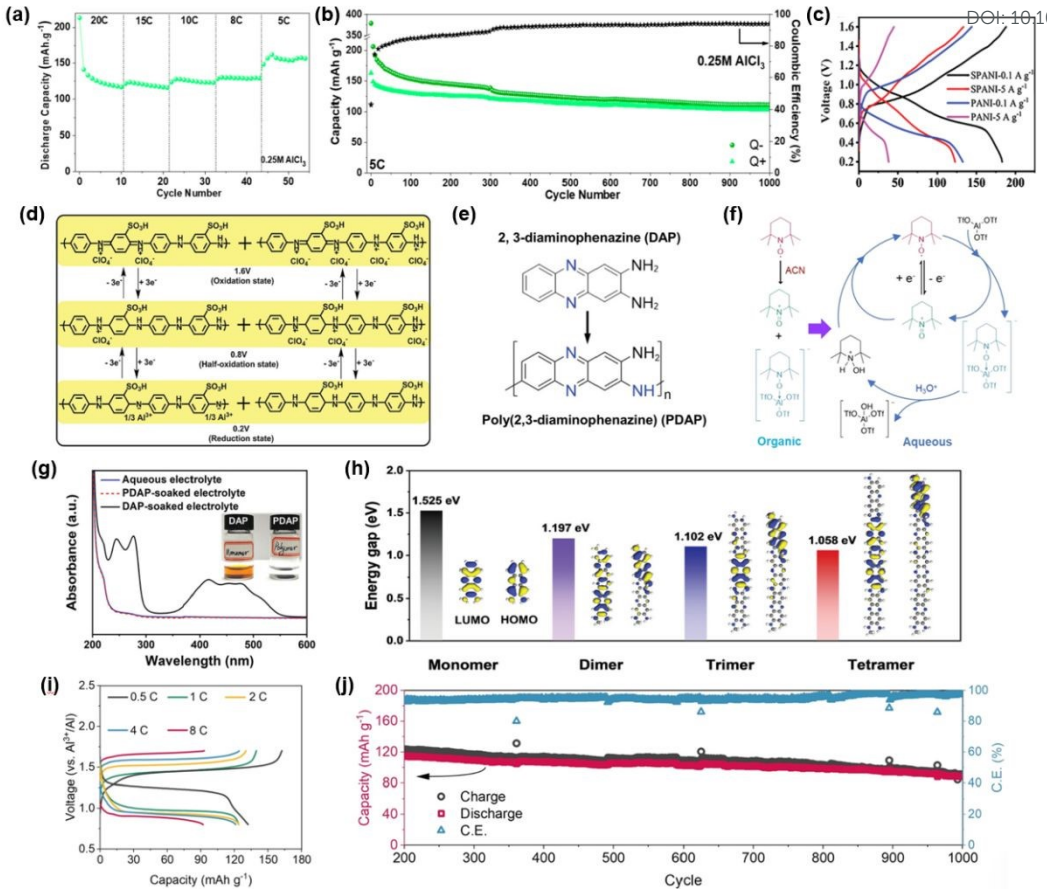

Figure 17 (a) C-rate performance in 0.25 M $AlCl_3$.(b) Long-term cycling performance at 5 C in 0.25 M $AlCl_3$. Reproduced with permission.[123] Copyright 2022, American Chemical Society. (c) The discharge/charge curves at different current densities and (d) Schematic diagram of the charge/discharge mechanism of the SPANI/ASHEE/Al battery. Reproduced with permission.[124] Copyright 2022, Wiley-VCH. (e) Illustration of the electropolymerization process of PDAP. (g) The UV-vis spectra of DAP-soaked, PDAP-soaked electrolyte, and fresh electrolyte (1 M $Al(ClO_4)_3$). (h) HOMO-LUMO energy gaps for the optimized models with different molecular chain length (monomer, dimer, trimer, and tetramer). Reproduced with permission.[125] Copyright 2024, Wiley-VCH. (f) Schematic illustration of the solvent-dependent redox behavior of TEMPO in acetonitrile and aqueous electrolytes. (i) typical charge/discharge voltage profiles of the PTMA cathodes cycled at 0.5 to 8 C. (j) Long cycling performance and Coulombic efficiency of PTMA-based AAIBs at 4C. Reproduced with permission.[129] Copyright 2023, American Chemical Society.

Table 1. Electrochemical performances of reported cathode materials for AAIBs.

Cathode material	Anode material	Electrolyte	Discharge voltage (V)	Current density (mA g^{-1})	Specific capacity (mAh g^{-1})	Cycle number	Ref.
α-MnO_2	Al	2 M $Al(OTf)_3$	1.3	100	380	40	[45]
α-MnO_2	Al	5 M $Al(OTf)_3$	1.5	100	480	180	[46]
γ-MnO_2	Al	5 M $Al(OTf)_3$	1.5	200	482	200	[47]
δ-MnO_2	Al	2 M $Al(OTf)_3$ + 0.5 M $MnSO_4$	1.35	100	554	65	[48]
δ-MnO_2	Pt-sputtered Al	5 M $Al(OTf)_3$	1.1	50	452	50	[49]
$Al_xMnO_2 \cdot nH_2O$	Al-Cu	2 M $Al(OTf)_3$	1.5	500	400	400	[51]
$Al_xMnO_2 \cdot nH_2O$	Al	5 M $Al(OTf)_3$	1.2	30	467	60	[52]
Al_xMnO_2	Zn-Al	2 M $Al(OTf)_3$	1.6	100	460	80	[53]
BQ-Al_xMnO_2	$Zn_{50}Al_{50}$ alloy	2 M $Al(OTf)_3$ + 0.2 M $Mn(OTf)_2$	1.6	1000	300	800	[55]
Cu^{2+}-pre-intercalated δ-MnO_2	Al	5 M $Al(OTf)_3$	1.5	400	363	300	[56]
Co-doped δ-MnO_2	Al	2 M $Al(OTf)_3$	1.4	100	585	300	[59]
V-doped δ-MnO_2	Al-Cu	2 M $Al(OTf)_3$	1.14	200	518	400	[60]
V_2O_5	Al	2 M $Al(OTf)_3$	0.9	20	200	50	[38]
V_2O_5	Al	5 M $Al(OTf)_3$	-	400	400	200	[65]
V_2O_5@MXene	Al	5 M $Al(OTf)_3$	-	100	626	100	[66]

View Article Online
DOI: 10.1039/D5SC09176D

VO_2	Al	5 M $Al(OTf)_3$	-	150	234	1000	[69]
Cu-doped VO_2	Al	5 M $Al(OTf)_3$	-	400	642	200	[71]
LiV_3O_8	activated carbon	2 M $Al(OTf)_3$	-	0.29 C	289	500	[72]
$VOPO_4 \cdot 2H_2O$	Al	2.5 M $Al(OTf)_3$	0.9	20	125	40	[80]
CuHCF	Graphite	0.5 M $Al_2(SO_4)_3$	-	50	63	1000	[90]
CuHCF	-	1 M $AlCl_3$	-	1000	54.5	5000	[93]
CuHCF	MoO_3	3 M $AlCl_3$	0.6	3000	48	150	[94]
FeFe-PBA	Deep eutectic-modified Al	2 M $Al(OTf)_3$	-	100	85	150	[96]
KNHCF	Al	5 M $Al(OTf)_3$	0.7	20	46.5	500	[97]
V-PBA	Zn	Deep eutectic	1.2	100	161	500	[98]
MnFe-PBA	Al	1 M $Al(OTf)_3$	0.9	200	106	50	[99]
medium-entropy PBA	MoO	3 M $Al(OTf)_3$	-	500	60.9	600	[101]
MgMn-PBA	MoO_3	1 M $Al(NO_3)_3$	-	1000	148	2000	[105]
Fe-Co PBA/rGO	MoO_3	1 M $AlCl_3$	-	100	112.5	1500	[106]
TCQ	Zn-Al	1 M $Al(OTf)_3$	-	200	148	200	[112]
C4Q	Al	1 M $Al(OTf)_3$	1.0	40	400	50	[113]
PZ	Al	5 M $Al(OTf)_3$	0.6	50	132	300	[114]

View Article Online
DOI: 10.1039/D5SC09176D

DPPZ-CN	Al	1 M $Al(ClO_4)_3$	0.6	100	212	1000	[116]
DQP-6CN	Al	5 M $Al(OTf)_3$	0.8	400	279	200	[117]
3BQ-CNT	Al	1 M $Al(OTf)_3$	-	50	446	4000	[118]
SPANI	Al	$Al(ClO_4)_3 \cdot 9H_2O$ + succinonitrile	0.5	100	185	300	[124]
PDAP	Al	1 M $Al(ClO_4)_3$	-	200	338	100	[125]
poly(TEMPO methacrylate)	Al	1 M $Al(OTf)_3$	1.1	4 C	120	800	[129]

View Article Online
DOI: 10.1039/D5SC09176D

Reference

1 J. Li, J. Fleetwood, W.B. Hawley, W. Kays, From Materials to Cell: State-of-the-Art and Prospective Technologies for Lithium-Ion Battery Electrode Processing. *Chem. Rev.* **2022,** *122*, 903-956.

2 A. Manthiram, A reflection on lithium-ion battery cathode chemistry. *Nat. Commun.* **2020,** *11*, 1550.

3 J. Xu, X. Cai, S. Cai, Y. Shao, C. Hu, S. Lu, S. Ding, High-Energy Lithium-Ion Batteries: Recent Progress and a Promising Future in Applications. *Energy Environ. Mater.* **2023,** *6*, e12450.

4 E.J.M. Dugamin, A. Richard, M. Cathelineau, M.C. Boiron, F. Despinois, A. Brisset, Groundwater in sedimentary basins as potential lithium resource: a global prospective study. *Scientific Reports* **2021,** *11*.

5 L. Han, L. Wang, Z. Chen, Y. Kan, Y. Hu, H. Zhang, X. He, Incombustible Polymer Electrolyte Boosting Safety of Solid-State Lithium Batteries: A Review. *Adv. Funct. Mater.* **2023,** *33*, 2300892.

6 Y. Chen, Y. Kang, Y. Zhao, L. Wang, J. Liu, Y. Li, Z. Liang, X. He, X. Li, N. Tavajohi, B. Li, A review of lithium-ion battery safety concerns: The issues, strategies, and testing standards. *J. Energy Chem.* **2021,** *59*, 83-99.

7 X. Gao, Y.-N. Zhou, D. Han, J. Zhou, D. Zhou, W. Tang, J.B. Goodenough, Thermodynamic Understanding of Li-Dendrite Formation. *Joule* **2020,** *4*, 1864-1879.

8 X. Cui, J. Wang, S. Sun, X. Chen, Y. Wang, D. Han, J. Wang, X. Yao, W. Yan, Safety Hazards of Lithium Metal Batteries: From the Perspective of Lithium Dendrites and Thermal Runaway. *Energy & Fuels* **2025,** *39*, 7665-7690.

9 P.K. Nayak, L. Yang, W. Brehm, P. Adelhelm, From Lithium-Ion to Sodium-Ion Batteries: Advantages, Challenges, and Surprises. *Angew. Chem. Int. Ed.* **2018,** *57*, 102-120.

10 T.L. Kulova, V.N. Fateev, E.A. Seregina, A.S. Grigoriev, A Brief Review of Post-Lithium-Ion Batteries. *International Journal of Electrochemical Science* **2020,** *15*, 7242-7259.

11 W. Du, E.H. Ang, Y. Yang, Y. Zhang, M. Ye, C.C. Li, Challenges in the material and structural design of zinc anode towards high-performance aqueous zinc-ion batteries. *Energy & Environmental Science* **2020,** *13*, 3330-3360.

12 D. Wang, Z. Zhang, Y. Hao, H. Jia, X. Shen, B. Qu, G. Huang, X. Zhou, J. Wang, C. Xu, F. Pan, Challenges and Progress in Rechargeable Magnesium-Ion Batteries: Materials, Interfaces, and Devices. *Adv. Funct. Mater.* **2024,** *34*, 2410406.

13 T. Dutta, J. Mary Gladis, Recent developments on electrode materials and electrolytes for aluminium-ion batteries. *Journal of Energy Storage* **2024,** *86*, 111287.

14 M. Ye, Y. Guan, R. Xu, P. Wang, Y. Zhang, J. Yu, D. Li, L. Li, Q. Zhao, Z. Wang, J. Liang, Y. Wu, Aqueous potassium-ion battery cathodes: Current status and prospects. *J. Energy Chem.* **2025,** *106*, 650-670.

15 H. Zhang, L. Qiao, M. Armand, Organic Electrolyte Design for Rechargeable Batteries: From Lithium to Magnesium. *Angew. Chem. Int. Ed.* **2022,** *61*, e202214054.

16 H. Aziam, B. Larhrib, C. Hakim, N. Sabi, H. Ben Youcef, I. Saadoune, Solid-state electrolytes for beyond lithium-ion batteries: A review. *Renewable and Sustainable Energy Reviews* **2022,** *167*, 112694.

17 A.A. Yaroshevsky, Abundances of chemical elements in the Earth's crust. *Geochemistry International* **2006,** *44*, 48-55.

18 X. Zheng, C. Han, C.-S. Lee, W. Yao, C. Zhi, Y. Tang, Materials challenges for aluminum ion based aqueous energy storage devices: Progress and prospects. *Prog. Mater Sci.* **2024,** *143*, 101253.

19 Y. Zhang, S. Liu, Y. Ji, J. Ma, H. Yu, Emerging Nonaqueous Aluminum-Ion Batteries: Challenges, Status, and Perspectives. *Adv. Mater.* **2018,** *30*, 1706310.

20 J. Tu, W.L. Song, H.P. Lei, Z.J. Yu, L.L. Chen, M.Y. Wang, S.Q. Jiao, Nonaqueous Rechargeable

Aluminum Batteries: Progresses, Challenges, and Perspectives. *Chem. Rev.* **2021,** *121*, 4903-4961.
21 B.-E. Jia, A.Q. Thang, C. Yan, C. Liu, C. Lv, Q. Zhu, J. Xu, J. Chen, H. Pan, Q. Yan, Rechargeable Aqueous Aluminum-Ion Battery: Progress and Outlook. *Small* **2022,** *18*, 2107773.
22 D. Chao, W. Zhou, F. Xie, C. Ye, H. Li, M. Jaroniec, S.-Z. Qiao, Roadmap for advanced aqueous batteries: From design of materials to applications. *Sci. Adv.* **2020,** *6*, eaba4098.
23 E. Levi, M.D. Levi, O. Chasid, D. Aurbach, A review on the problems of the solid state ions diffusion in cathodes for rechargeable Mg batteries. *J. Electroceram.* **2009,** *22*, 13-19.
24 F. Wu, H. Yang, Y. Bai, C. Wu, Paving the Path toward Reliable Cathode Materials for Aluminum-Ion Batteries. *Adv. Mater.* **2019,** *31*, 1806510.
25 D. Ma, J. Li, H. Li, D. Yuan, Z. Ji, M. Manawan, C.P. de León Albarran, C. Wu, J.H. Pan, Progress of Advanced Cathode Materials of Rechargeable Aluminum-Ion Batteries. *Energy Material Advances* **2024,** *5*, 0088.
26 K. Bhimani, A. Anjan, V. Mahajani, R.M. Manoj, N. Koratkar, Tuning the Aluminum–Water Interface in Aqueous Aluminum Metal Batteries. *ACS Applied Energy Materials* **2025,** *8*, 6194-6202.
27 X. Geng, X. Hou, X. He, H.J. Fan, Challenges and Strategies on Interphasial Regulation for Aqueous Rechargeable Batteries. *Advanced Energy Materials* **2024,** *14*, 2304094.
28 S. Chen, N.A. Gadelhak, Y. Wu, J. Feng, C. Yu, X. Huang, A.K. Nanjundan, Aqueous Aluminium-Ion Batteries: Cathode Material Design, Anode Engineering and Electrolyte Innovation. *Small* **2025**, e07888.
29 R. Mori, Aqueous rechargeable aluminum battery - a mini review. *Energy Advances* **2025,** *4*.
30 H. Sun, B. Chen, M. Tan, Y. Li, X. Lang, Q. Jiang, Rational design and construction of aqueous multivalent metal ion battery systems. *J. Mater. Chem. A* **2025,** *13*, 17159-17196.
31 V. Mathew, B. Sambandam, S. Kim, S. Kim, S. Park, S. Lee, M.H. Alfaruqi, V. Soundharrajan, S. Islam, D.Y. Putro, J.-Y. Hwang, Y.-K. Sun, J. Kim, Manganese and Vanadium Oxide Cathodes for Aqueous Rechargeable Zinc-Ion Batteries: A Focused View on Performance, Mechanism, and Developments. *ACS Energy Letters* **2020,** *5*, 2376-2400.
32 Y. Xu, G. Zhang, J. Liu, J. Zhang, X. Wang, X. Pu, J. Wang, C. Yan, Y. Cao, H. Yang, W. Li, X. Li, Recent Advances on Challenges and Strategies of Manganese Dioxide Cathodes for Aqueous Zinc-Ion Batteries. *Energy Environ. Mater.* **2023,** *6*, e12575.
33 R. Liu, Z. Liang, Y. Xiang, W. Zhao, H. Liu, Y. Chen, K. An, Recognition of V/V/V Multielectron Reactions in Na3V(PO4)2: A Potential High Energy Density Cathode for Sodium-Ion Batteries. *Molecules* **2020,** *25*, 1000.
34 P.M. Hari Prasad, G. Malavika, A. Pillai, S. Sadan, Z.S. Pillai, Emerging organic electrode materials for sustainable batteries. *NPG Asia Materials* **2024,** *16*, 37.
35 Z. Song, H. Zhou, Towards sustainable and versatile energy storage devices: an overview of organic electrode materials. *Energy & Environmental Science* **2013,** *6*, 2280-2301.
36 X. Wang, Z. Xi, Q. Zhao, Progress on aqueous rechargeable aluminium metal batteries. *Industrial Chemistry & Materials* **2024,** *3*, 7-30.
37 H. Liu, Q. Zhou, Q. Xia, Y. Lei, X. Long Huang, M. Tebyetekerwa, X. Song Zhao, Interface challenges and optimization strategies for aqueous zinc-ion batteries. *J. Energy Chem.* **2023,** *77*, 642-659.
38 Q. Zhao, L. Liu, J. Yin, J. Zheng, D. Zhang, J. Chen, L.A. Archer, Proton Intercalation/De-Intercalation Dynamics in Vanadium Oxides for Aqueous Aluminum Electrochemical Cells. *Angew. Chem., Int. Ed.* **2020,** *59*, 3048.

39 X. Luo, R. Wang, L. Zhang, Z. Liu, H. Li, J. Mao, S. Zhang, J. Hao, T. Zhou, C. Zhang, Air-Stable and Low-Cost High-Voltage Hydrated Eutectic Electrolyte for High-Performance Aqueous Aluminum-Ion Rechargeable Battery with Wide-Temperature Range. *ACS Nano* **2024,** *18*, 12981-12993.

40 Y. Guo, Y. Zhang, H. Lu, Manganese-based materials as cathode for rechargeable aqueous zinc-ion batteries. *Battery Energy* **2022,** *1*, 20210014.

41 B. Zhang, P. Dong, S. Yuan, Y. Zhang, Y. Zhang, Y. Wang, Manganese-Based Oxide Cathode Materials for Aqueous Zinc-Ion Batteries: Materials, Mechanism, Challenges, and Strategies. *Chem & Bio Engineering* **2024,** *1*, 113-132.

42 Y. Yuan, C. Liu, B.W. Byles, W. Yao, B. Song, M. Cheng, Z. Huang, K. Amine, E. Pomerantseva, R. Shahbazian-Yassar, J. Lu, Ordering Heterogeneity of [MnO6] Octahedra in Tunnel-Structured MnO2 and Its Influence on Ion Storage. *Joule* **2019,** *3*, 471-484.

43 O. Ghodbane, J.-L. Pascal, B. Fraisse, F. Favier, Structural in Situ Study of the Thermal Behavior of Manganese Dioxide Materials: Toward Selected Electrode Materials for Supercapacitors. *ACS Appl. Mater. Interfaces* **2010,** *2*, 3493-3505.

44 D. Wang, L. Wang, G. Liang, H. Li, Z. Liu, Z. Tang, J. Liang, C. Zhi, A Superior δ-MnO2 Cathode and a Self-Healing Zn-δ-MnO2 Battery. *ACS Nano* **2019,** *13*, 10643-10652.

45 Q. Zhao, M.J. Zachman, W.I. Al Sadat, J. Zheng, L.F. Kourkoutis, L. Archer, Solid electrolyte interphases for high-energy aqueous aluminum electrochemical cells. *Sci. Adv.* **2018,** *4*, eaau8131.

46 X. Yang, Q. Sun, L. Chai, S. Chen, W. Zhang, H.Y. Yang, Z. Li, α-MnO2 Cathode with Oxygen Vacancies Accelerated Affinity Electrolyte for Dual-Ion Co-Encapsulated Aqueous Aluminum Ion Batteries. *Small* **2024,** *20*, 2400335.

47 H. Gu, X. Yang, S. Chen, W. Zhang, H.Y. Yang, Z. Li, Oxygen Vacancies Boosted Proton Intercalation Kinetics for Aqueous Aluminum–Manganese Batteries. *Nano Lett.* **2023,** *23*, 11842-11849.

48 S. He, J. Wang, X. Zhang, J. Chen, Z. Wang, T. Yang, Z. Liu, Y. Liang, B. Wang, S. Liu, L. Zhang, J. Huang, J. Huang, L.A. O'Dell, H. Yu, A High-Energy Aqueous Aluminum-Manganese Battery. *Adv. Funct. Mater.* **2019,** *29*, 1905228.

49 G. Li, Y. Zhao, B. Guo, J. Zhang, J. Jia, A. Wang, C. Liu, Architecting a High Specific Energy Aqueous Aluminum–Manganese Battery. *Battery Energy* **2025**, e70016.

50 C. Yan, C. Lv, B.-E. Jia, L. Zhong, X. Cao, X. Guo, H. Liu, W. Xu, D. Liu, L. Yang, J. Liu, H.H. Hng, W. Chen, L. Song, S. Li, Z. Liu, Q. Yan, G. Yu, Reversible Al Metal Anodes Enabled by Amorphization for Aqueous Aluminum Batteries. *J. Am. Chem. Soc.* **2022,** *144*, 11444-11455.

51 Q. Ran, H. Shi, H. Meng, S.-P. Zeng, W.-B. Wan, W. Zhang, Z. Wen, X.-Y. Lang, Q. Jiang, Aluminum-copper alloy anode materials for high-energy aqueous aluminum batteries. *Nat. Commun.* **2022,** *13*, 576.

52 C. Wu, S. Gu, Q. Zhang, Y. Bai, M. Li, Y. Yuan, H. Wang, X. Liu, Y. Yuan, N. Zhu, F. Wu, H. Li, L. Gu, J. Lu, Electrochemically activated spinel manganese oxide for rechargeable aqueous aluminum battery. *Nat. Commun.* **2019,** *10*, 73.

53 C. Yan, C. Lv, L. Wang, W. Cui, L. Zhang, K.N. Dinh, H. Tan, C. Wu, T. Wu, Y. Ren, J. Chen, Z. Liu, M. Srinivasan, X. Rui, Q. Yan, G. Yu, Architecting a Stable High-Energy Aqueous Al-Ion Battery. *J. Am. Chem. Soc.* **2020,** *142*, 15295-15304.

54 Y. Liu, G. He, H. Jiang, I.P. Parkin, P.R. Shearing, D.J.L. Brett, Cathode Design for Aqueous Rechargeable Multivalent Ion Batteries: Challenges and Opportunities. *Adv. Funct. Mater.* **2021,** *31*, 2010445.

55 H. Meng, Q. Ran, M.-H. Zhu, Q.-Z. Zhao, G.-F. Han, T.-H. Wang, Z. Wen, X.-Y. Lang, Q. Jiang,

Benzoquinone-Lubricated Intercalation in Manganese Oxide for High-Capacity and High-Rate Aqueous Aluminum-Ion Battery. *Small* **2024,** *20*, 2310722.

56 H. Gu, M. Chen, Z. Wang, W. Zhang, Z. Li, Enhancing H+ intercalation kinetics and stability in Cu2+ pre-intercalated δ-MnO2 for aqueous aluminum batteries. *J. Energy Chem.* **2025,** *102*, 126-133.

57 A. Zhang, Y. Liang, H. Zhang, Z. Geng, J. Zeng, Doping regulation in transition metal compounds for electrocatalysis. *Chem. Soc. Rev.* **2021,** *50*, 9817-9844.

58 P. Gao, Z. Chen, Y. Gong, R. Zhang, H. Liu, P. Tang, X. Chen, S. Passerini, J. Liu, The Role of Cation Vacancies in Electrode Materials for Enhanced Electrochemical Energy Storage: Synthesis, Advanced Characterization, and Fundamentals. *Advanced Energy Materials* **2020,** *10*, 1903780.

59 J. Yang, W. Gong, F. Geng, Defect Modulation in Cobalt Manganese Oxide Sheets for Stable and High-Energy Aqueous Aluminum-Ion Batteries. *Adv. Funct. Mater.* **2023,** *33*, 2301202.

60 S. Chen, Y. Kong, C. Tang, N.A. Gadelhak, A.K. Nanjundan, A. Du, C. Yu, X. Huang, Doping Regulation Stabilizing δ-MnO2 Cathode for High-Performance Aqueous Aluminium-ion Batteries. *Small* **2024,** *20*, 2312229.

61 B. Baatiyah, Y.S. Wudil, M.A. Gondal, Recent advances and challenges in MnO_2-based composite cathodes for high-performance flexible zinc-ion batteries: A critical review. *Journal of Energy Storage* **2025,** *125*, 117000.

62 Y. Hu, H. Li, H. Gu, W. Zhang, Z. Li, Al3+ pre-intercalation and g-C3N4 coating synergistically modulate gibbs free energy for robust and compatible MnO2 cathodes in aqueous aluminum batteries. *Chem. Eng. J.* **2025,** *507*, 160532.

63 J.R. González, F. Nacimiento, M. Cabello, R. Alcántara, P. Lavela, J.L. Tirado, Reversible intercalation of aluminium into vanadium pentoxide xerogel for aqueous rechargeable batteries. *RSC Adv.* **2016,** *6*, 62157-62164.

64 P. De, J. Halder, S. Priya, A.K. Srivastava, A. Chandra, Two-Dimensional V2O5 Nanosheets as an Advanced Cathode Material for Realizing Low-Cost Aqueous Aluminum-Ion Batteries. *ACS Applied Energy Materials* **2023,** *6*, 753-762.

65 Z. Wang, H. Gu, T. Wu, W. Zhang, Z. Li, Enhanced dynamics of Al3+/H+ ions in aqueous aluminum ion batteries: Construction of metastable structures in vanadium pentoxide upon oxygen vacancies. *J. Energy Chem.* **2025,** *101*, 562-569.

66 X. Yang, H. Gu, L. Chai, S. Chen, W. Zhang, H.Y. Yang, Z. Li, Construction of V2O5@MXene Cathodes toward a High Specific Capacity Aqueous Aluminum-Ion Battery. *Nano Lett.* **2024,** *24*, 8542-8549.

67 S. Lee, X.-G. Sun, A.A. Lubimtsev, X. Gao, P. Ganesh, T.Z. Ward, G. Eres, M.F. Chisholm, S. Dai, H.N. Lee, Persistent Electrochemical Performance in Epitaxial VO2(B). *Nano Lett.* **2017,** *17*, 2229-2233.

68 Q. He, T. Hu, Q. Wu, C. Wang, X. Han, Z. Chen, Y. Zhu, J. Chen, Y. Zhang, L. Shi, X. Wang, Y. Ma, J. Zhao, Tunnel-Oriented VO2 (B) Cathode for High-Rate Aqueous Zinc-Ion Batteries. *Adv. Mater.* **2024,** *36*, 2400888.

69 Y. Cai, S. Kumar, R. Chua, V. Verma, D. Yuan, Z. Kou, H. Ren, H. Arora, M. Srinivasan, Bronze-type vanadium dioxide holey nanobelts as high performing cathode material for aqueous aluminium-ion batteries. *J. Mater. Chem. A* **2020,** *8*, 12716-12722.

70 Y. Wang, X. Shi, J. Wang, X. Liu, X. Lu, Nanobelt-like vanadium dioxide with three-dimensional interconnected tunnel structure enables ultrafast Al-ion storage. *Materials Today Energy* **2021,** *19*, 100578.

71 Z. Wang, H. Gu, Z. Li, Orbital-Modulated Cu-Doped VO2 Nanoflowers via Glucose-Assisted

Synthesis: Structural Optimization and Electronic Coupling Engineering for High-Capacity Aqueous Aluminum Ion Batteries. *Small* **2025,** *21*, 2503861.

72 V. Soundharrajan, S. Nithiananth, J. Lee, J.H. Kim, J.-Y. Hwang, J. Kim, LiV3O8 as an intercalation-type cathode for aqueous aluminum-ion batteries. *J. Mater. Chem. A* **2022,** *10*, 18162-18169.

73 R. Liu, J. Liu, Y. Li, C. Zhang, H. Li, Aqueous aluminum-ion batteries based on layered NH4V4O10 nanosheets as cathode. *Solid State Sciences* **2023,** *145*, 107315.

74 V.P.H. Radhakantha, S. Pradhan, A.J. Bhattacharyya, Exploring Aluminum-Ion (Al3+) Insertion in Ammonium Vanadium Bronze (NH4V4O10) for Aqueous Aluminum-Ion Rechargeable Batteries. *The Journal of Physical Chemistry C* **2024,** *128*, 20025-20034.

75 T. Wu, Y. Wang, Z. Wang, W. Zhang, Z. Li, Achieving (NH4)2V10O25·8H2O reversible stable phase transition, fast energy storage, and dynamic characteristics with MXene for aqueous aluminum batteries. *Chem. Eng. J.* **2024,** *499*, 155926.

76 X. Xu, F. Xiong, J. Meng, X. Wang, C. Niu, Q. An, L. Mai, Vanadium-Based Nanomaterials: A Promising Family for Emerging Metal-Ion Batteries. *Adv. Funct. Mater.* **2020,** *30*, 1904398.

77 A. Kraytsberg, Y. Ein-Eli, Higher, Stronger, Better ... A Review of 5 Volt Cathode Materials for Advanced Lithium-Ion Batteries. *Advanced Energy Materials* **2012,** *2*, 922-939.

78 F. Nacimiento, M. Cabello, R. Alcántara, P. Lavela, J.L. Tirado, NASICON-type Na3V2(PO4)3 as a new positive electrode material for rechargeable aluminium battery. *Electrochim. Acta* **2018,** *260*, 798-804.

79 P. Wang, Z. Chen, H. Wang, Z. Ji, Y. Feng, J. Wang, J. Liu, M. Hu, J. Fei, W. Gan, Y. Huang, A high-performance flexible aqueous Al ion rechargeable battery with long cycle life. *Energy Storage Materials* **2020,** *25*, 426-435.

80 Q. Pang, S. Yang, X. Yu, W. He, S. Zhang, Y. Tian, M. Xing, Y. Fu, X. Luo, Realizing reversible storage of trivalent aluminum ions using VOPO4·2H2O nanosheets as cathode material in aqueous aluminum metal batteries. *J. Alloys Compd.* **2021,** *885*, 161008.

81 Y. Liu, J.-L. Yang, H.-H. Liu, J.-M. Cao, Y. Liu, X.-L. Wu, Effective reversible calcium/aluminum ion intercalation into VOPO4 enabled by organic molecular assistance. *J. Mater. Chem. A* **2025,** *13*, 17404-17410.

82 C.D. Wessells, S.V. Peddada, R.A. Huggins, Y. Cui, Nickel Hexacyanoferrate Nanoparticle Electrodes For Aqueous Sodium and Potassium Ion Batteries. *Nano Lett.* **2011,** *11*, 5421-5425.

83 C.D. Wessells, R.A. Huggins, Y. Cui, Copper hexacyanoferrate battery electrodes with long cycle life and high power. *Nat. Commun.* **2011,** *2*, 550.

84 J. Peng, W. Zhang, Q. Liu, J. Wang, S. Chou, H. Liu, S. Dou, Prussian Blue Analogues for Sodium-Ion Batteries: Past, Present, and Future. *Adv. Mater.* **2022,** *34*, 2108384.

85 Q. Liu, Z. Hu, M. Chen, C. Zou, H. Jin, S. Wang, S.-L. Chou, Y. Liu, S.-X. Dou, The Cathode Choice for Commercialization of Sodium-Ion Batteries: Layered Transition Metal Oxides versus Prussian Blue Analogs. *Adv. Funct. Mater.* **2020,** *30*, 1909530.

86 X.-Y. Fu, L.-L. Zhang, C.-C. Wang, H.-B. Sun, X.-L. Yang, Recent progress of Prussian blue analogues as cathode materials for metal ion secondary batteries. *Rare Metals* **2025,** *44*, 34-59.

87 J. Song, L. Wang, Y. Lu, J. Liu, B. Guo, P. Xiao, J.-J. Lee, X.-Q. Yang, G. Henkelman, J.B. Goodenough, Removal of Interstitial H2O in Hexacyanometallates for a Superior Cathode of a Sodium-Ion Battery. *J. Am. Chem. Soc.* **2015,** *137*, 2658-2664.

88 W. Wang, Y. Gang, J. Peng, Z. Hu, Z. Yan, W. Lai, Y. Zhu, D. Appadoo, M. Ye, Y. Cao, Q.-F. Gu, H.-K. Liu, S.-X. Dou, S.-L. Chou, Effect of Eliminating Water in Prussian Blue Cathode for Sodium-Ion

View Article Online
DOI: 10.1039/D5SC09176D

Batteries. *Adv. Funct. Mater.* **2022,** *32*, 2111727.

89 Z. Li, K. Xiang, W. Xing, W.C. Carter, Y.-M. Chiang, Reversible Aluminum-Ion Intercalation in Prussian Blue Analogs and Demonstration of a High-Power Aluminum-Ion Asymmetric Capacitor. *Advanced Energy Materials* **2015,** *5*, 1401410.

90 S. Liu, G.L. Pan, G.R. Li, X.P. Gao, Copper hexacyanoferrate nanoparticles as cathode material for aqueous Al-ion batteries. *J. Mater. Chem. A* **2015,** *3*, 959-962.

91 Z. Zhao, W. Zhang, M. Liu, S.J. Yoo, N. Yue, F. Liu, X. Zhou, K. Song, J.-G. Kim, Z. Chen, X.-Y. Lang, Q. Jiang, C. Zhi, W. Zheng, Ultrafast Nucleation Reverses Dissolution of Transition Metal Ions for Robust Aqueous Batteries. *Nano Lett.* **2023,** *23*, 5307-5316.

92 V.P.H. Radhakantha, J. Tiongson, U.S. Manjunatha, L. O'Dell, A.J. Bhattacharyya, The critical impact of electrolyte concentration on Al3+ redox and stability of CuHCF in aqueous aluminum-ion batteries. *J. Mater. Chem. A* **2026**.

93 J. Zheng, D. Li, Z. Feng, Y. Wang, T. Sun, Preintercalated Copper Hexacyanoferrate as a Long-Time Cycle Cathode Material for Aqueous Aluminum-Ion Batteries. *ACS Sustainable Chemistry & Engineering* **2023,** *11*, 6280-6291.

94 K. Sayeed, A. Sadhanala, C.V. Yelamaggad, K. Pandey, Inceptive high-performance flexible aqueous aluminum-ion batteries derived from pre-intercalated copper hexacyanoferrate cathode. *Journal of Energy Storage* **2025,** *132*, 117881.

95 A. Zhou, L. Jiang, J. Yue, Y. Tong, Q. Zhang, Z. Lin, B. Liu, C. Wu, L. Suo, Y.S. Hu, H. Li, L. Chen, Water-in-Salt Electrolyte Promotes High-Capacity FeFe(CN)(6) Cathode for Aqueous Al-Ion Battery. *ACS Appl. Mater. Interfaces* **2019,** *11*, 41356-41362.

96 R. Bai, J. Yang, G. Li, J. Luo, W. Tang, Rechargeable aqueous aluminum-FeFe(CN)6 battery with artificial interphase through deep eutectic solution. *Energy Storage Materials* **2021,** *41*, 41-50.

97 Y. Gao, H. Yang, X. Wang, Y. Bai, N. Zhu, S. Guo, L. Suo, H. Li, H. Xu, C. Wu, The Compensation Effect Mechanism of Fe–Ni Mixed Prussian Blue Analogues in Aqueous Rechargeable Aluminum-Ion Batteries. *ChemSusChem* **2020,** *13*, 732-740.

98 W. Feng, B. Li, G. Yuan, Y. Li, Y. Zhang, M. Du, Y. Su, Y. Tang, H. Yue, Y. Li, M. Shakouri, H.-C. Chen, W. Li, Z. Liu, H. Pang, High Performance Aluminum Ion Batteries Enabled by the Coordination Between Vanadium-Based PBAs Cathode and Aqueous Eutectic Electrolyte. *Adv. Sci.* **2025**, e11274.

99 D. Wang, H. Lv, T. Hussain, Q. Yang, G. Liang, Y. Zhao, L. Ma, Q. Li, H. Li, B. Dong, T. Kaewmaraya, C. Zhi, A manganese hexacyanoferrate framework with enlarged ion tunnels and two-species redox reaction for aqueous Al-ion batteries. *Nano Energy* **2021,** *84*, 105945.

100 W. Shang, Y. Liu, Y.-N. Liu, J.-L. Yang, H.-H. Liu, H. Yu, J.-M. Cao, X.-L. Wu, Lattice Distortion Confinement Induced by Cationic Vacancy for Ambient Temperature Durable Aluminum-Ion Batteries. *Adv. Funct. Mater.* **2025,** *35*, 2422805.

101 Y.-N. Liu, J.-L. Yang, Z.-Y. Gu, X.-Y. Zhang, Y. Liu, M.-Y. Su, X.-L. Zhang, I.V. Zatovsky, K. Li, J.-M. Cao, X.-L. Wu, Entropy-Regulated Cathode with Low Strain and Constraint Phase-Change Toward Ultralong-Life Aqueous Al-Ion Batteries. *Angew. Chem. Int. Ed.* **2024,** *63*, e202316925.

102 K. Du, Y. Liu, Y. Zhao, H. Li, H. Liu, C. Sun, M. Han, T. Ma, Y. Hu, High-Entropy Prussian Blue Analogues Enable Lattice Respiration for Ultrastable Aqueous Aluminum-Ion Batteries. *Adv. Mater.* **2024,** *36*, 2404172.

103 Y. Ru, S. Zheng, H. Xue, H. Pang, Potassium cobalt hexacyanoferrate nanocubic assemblies for high-performance aqueous aluminum ion batteries. *Chem. Eng. J.* **2020,** *382*, 122853.

104 J. Zheng, J. Liu, M. Ma, R. Zhang, S. Zhang, Y. Wang, T. Sun, Prussian Blue Analogue-Based Nanowires as Cathode Materials for Aqueous Aluminum-Ion Storage. *ACS Applied Nano Materials* **2024,** *7*, 28659-28668.

105 W. Chang, J. Peng, W. Mao, Q. Wang, Y. Zhu, N. Peng, Mg-Substituted dual-walled Prussian blue analogous achieving enhanced active sites and stability for aqueous Al-ion batteries. *Chem. Eng. J.* **2024,** *500*, 157204.

106 A. Zhao, J. Peng, W. Mao, Q. Wang, Y. Zhu, N. Peng, Fe-Co PBA/rGO interface strategy enabling fast Al3+ intercalation for stable aqueous Al-ion batteries. *Chem. Eng. J.* **2024,** *493*, 152790.

107 Y. Lu, Q. Zhang, L. Li, Z. Niu, J. Chen, Design Strategies toward Enhancing the Performance of Organic Electrode Materials in Metal-Ion Batteries. *Chem* **2018,** *4*, 2786-2813.

108 Y. Qi, H. Zhao, Y. Lei, Organic molecular design for high-power density sodium-ion batteries. *Chem. Commun.* **2025,** *61*, 2375-2386.

109 W. Walker, S. Grugeon, O. Mentre, S. Laruelle, J.-M. Tarascon, F. Wudl, Ethoxycarbonyl-Based Organic Electrode for Li-Batteries. *J. Am. Chem. Soc.* **2010,** *132*, 6517-6523.

110 Y. Liang, Y. Jing, S. Gheytani, K.-Y. Lee, P. Liu, A. Facchetti, Y. Yao, Universal quinone electrodes for long cycle life aqueous rechargeable batteries. *Nat. Mater.* **2017,** *16*, 841-848.

111 X. Peng, Y. Xie, A. Baktash, J. Tang, T. Lin, X. Huang, Y. Hu, Z. Jia, D.J. Searles, Y. Yamauchi, L. Wang, B. Luo, Heterocyclic Conjugated Polymer Nanoarchitectonics with Synergistic Redox-Active Sites for High-Performance Aluminium Organic Batteries. *Angew. Chem. Int. Ed.* **2022,** *61*, e202203646.

112 J. He, X. Shi, C. Wang, H. Zhang, X. Liu, Z. Yang, X. Lu, A quinone electrode with reversible phase conversion for long-life rechargeable aqueous aluminum–metal batteries. *Chem. Commun.* **2021,** *57*, 6931-6934.

113 Y. Li, L. Liu, Y. Lu, R. Shi, Y. Ma, Z. Yan, K. Zhang, J. Chen, High-Energy-Density Quinone-Based Electrodes with [Al(OTF)]2+ Storage Mechanism for Rechargeable Aqueous Aluminum Batteries. *Adv. Funct. Mater.* **2021,** *31*, 2102063.

114 J. Chen, Q. Zhu, L. Jiang, R. Liu, Y. Yang, M. Tang, J. Wang, H. Wang, L. Guo, Rechargeable Aqueous Aluminum Organic Batteries. *Angew. Chem. Int. Ed.* **2021,** *60*, 5794-5799.

115 J. Cui, Z. Guo, J. Yi, X. Liu, K. Wu, P. Liang, Q. Li, Y. Liu, Y. Wang, Y. Xia, J. Zhang, Organic Cathode Materials for Rechargeable Zinc Batteries: Mechanisms, Challenges, and Perspectives. *ChemSusChem* **2020,** *13*, 2160-2185.

116 H. Li, M. Cao, R. Wang, P. Xiong, Y. Liu, L. Zhang, L. Zhang, L. Zhang, D. Chao, C. Zhang, Design Strategy for Small-Molecule Organic Cathodes: Regulated Active Groups Enable High Capacity and Voltage in Aqueous and Seawater Aluminum Ion Batteries. *Angew. Chem. Int. Ed.* **2025,** *64*, e202508057.

117 Y. Lu, Q. Ge, C. Hu, H. Chen, W. Zhang, Z. Li, An π-conjugated organic cathode with multiple cyano-substituted for stable aqueous aluminum batteries. *J. Colloid Interface Sci.* **2025,** *682*, 281-287.

118 J. Su, M. Zhang, H. Tian, M. Han, Z. Sun, K. Du, F. Cui, J. Li, W. Huang, Y. Hu, Synergistic π-Conjugation Organic Cathode for Ultra-Stable Aqueous Aluminum Batteries. *Small* **2024,** *20*, 2312086.

119 Y. Lu, C. Hu, Y. Hu, W. Zhang, Z. Li, Carbonyl and imine conjugated frameworks for aqueous Organo-Aluminum batteries with high specific capacity and low dissolution. *J. Colloid Interface Sci.* **2024,** *665*, 181-187.

120 C. Hu, Y. Lu, H. Gu, W. Zhang, Z. Li, Multiple Redox Site π-Conjugated Materials for Aqueous Aluminum–Organic Battery Cathodes. *ACS Energy Letters* **2024,** *9*, 4353-4360.

121 F. Wan, L. Zhang, X. Wang, S. Bi, Z. Niu, J. Chen, An Aqueous Rechargeable Zinc-Organic Battery with Hybrid Mechanism. *Adv. Funct. Mater.* **2018,** *28*, 1804975.

DOI: 10.1039/D5SC09176D

122 X. Li, X. Xie, R. Lv, B. Na, B. Wang, Y. He, Nanostructured Polypyrrole Composite Aerogels for a Rechargeable Flexible Aqueous Zn-Ion Battery with High Rate Capabilities. *Energy Technology* **2019,** *7*, 1801092.

123 S. Sariyer, A. Ghosh, S.N. Dambasan, E.M. Halim, M. El Rhazi, H. Perrot, O. Sel, R. Demir-Cakan, Aqueous Multivalent Charge Storage Mechanism in Aromatic Diamine-Based Organic Electrodes. *ACS Appl. Mater. Interfaces* **2022,** *14*, 8508-8520.

124 P. Meng, J. Huang, Z. Yang, F. Wang, T. Lv, J. Zhang, C. Fu, W. Xiao, A Low-Cost and Air-Stable Rechargeable Aluminum-Ion Battery. *Adv. Mater.* **2022,** *34*, 2106511.

125 W. Wang, S. Zhang, L. Zhang, R. Wang, Q. Ma, H. Li, J. Hao, T. Zhou, J. Mao, C. Zhang, Electropolymerized Bipolar Poly(2,3-diaminophenazine) Cathode for High-Performance Aqueous Al-Ion Batteries with An Extended Temperature Range of −20 to 45 °C. *Adv. Mater.* **2024,** *36*, 2400642.

126 Y. Xiong, Y. Li, X. Cui, S. Li, X. Peng, Y. Ju, T. Zhou, R. Feng, Y. Zhang, Z. Wang, Q. Wang, L. Dong, Stable Radical Polymers as New Electroactive Materials: Synthesis, Properties, and Emerging Applications. *Adv. Funct. Mater.* **2025,** *35*, 2419661.

127 D.R. Nevers, F.R. Brushett, D.R. Wheeler, Engineering radical polymer electrodes for electrochemical energy storage. *J. Power Sources* **2017,** *352*, 226-244.

128 K. Sato, R. Ichinoi, R. Mizukami, T. Serikawa, Y. Sasaki, J. Lutkenhaus, H. Nishide, K. Oyaizu, Diffusion-Cooperative Model for Charge Transport by Redox-Active Nonconjugated Polymers. *J. Am. Chem. Soc.* **2018,** *140*, 1049-1056.

129 S. Jiang, Y. Xie, Y. Xie, L.-J. Yu, X. Yan, F.-G. Zhao, C.J. Mudugamuwa, M.L. Coote, Z. Jia, K. Zhang, Lewis Acid-Induced Reversible Disproportionation of TEMPO Enables Aqueous Aluminum Radical Batteries. *J. Am. Chem. Soc.* **2023,** *145*, 14519-14528.

View Article Online
DOI: 10.1039/D5SC09176D

Data availability

No primary research results, software or code have been included and no new data were generated or analysed as part of this review.